2004: The Journal of Astronomical Data 10, 2.

High-resolution spectroscopy of the eclipsing β Cephei star HD 92024*

H. Hensberge[1], C. Sterken[2†], L.M. Freyhammer[1,2], K. Pavlovski[3], S. Ilijić[4] and A. Smette[5,6‡]

(1) Royal Observatory of Belgium, Ringlaan 3, B-1180 Brussels, Belgium (2) Vrije Universiteit Brussel, Pleinlaan 2, B-1050 Brussels, Belgium (3) Dept. of Physics, University of Zagreb, Bijenička 32, HR-10000 Zagreb, Croatia (4) Fac. of Electrical Engineering and Computing, Dept. of Applied Physics, University of Zagreb, Unska 3, HR-10000 Zagreb, Croatia (5) Institut d'Astrophysique et de Géophysique, Université de Liège, 17 Allée du 6 Août, B-4000 Liège, Belgium, (6) European Southern Observatory, Casilla 19001, Vitacura, Santiago, Chile

Received 6 September 2004; Accepted 22 October 2004

Abstract

We present spectroscopic data from a recent orbital analysis of the eclipsing SB1 type binary system HD 92024 which has a β Cephei component. Fully reduced spectra are given together with technical details from the analysis, published elsewhere. In addition, a high-S/N time-averaged spectrum with line identifications is provided in graphical and digital form. The spectra show pronounced pulsational variability, which is essential for application in asteroseismology but disturbing for the dynamical analysis. Orbital elements derived from the spectra with a procedure devised to minimise influence from these line-profile variations are found to be more precise

*Based on observations obtained at the European Southern Observatory at La Silla, Chile (Applications 66.D-0297(A), 67.D-0023(A), 68.D-0280(A))

†Research Director, Belgian Fund for Scientific Research (FWO)

‡Research Associate, Belgian National Fund for Scientific Research (FNRS)

than orbital parameters resulting from classical methods. A line-variability indicator is described and then used to guide a selection of spectral line-regions rich in information on the stellar β Cephei oscillations. Two lines are examined as examples.

Keywords: Binaries: eclipsing : spectroscopic – variable stars: β Cephei type – clusters : NGC 3293 – spectroscopy : echelle : techniques : data reduction

1 Introduction

In 1989, several spectra were obtained over 50% of the orbital phases of HD 92024 (V381 Car, B1 III, $m_V = 9.02$), a rare eclipsing binary system with a β Cephei component (only one other case is known: EN(16) Lac, Jerzykiewicz et al. 1978). Much later, in 2001, during an observing run with FEROS at the ESO 1.52 m telescope we obtained a similar number of high-quality spectra of HD 92024. The new spectra, having shorter exposure times, revealed large and fast line variability compared to the 8.3245 d orbit (Jerzykiewicz and Sterken 1992, JS92 hereafter). In 2002, we were granted 4 nights observing time dedicated to this system. A profound analysis (Freyhammer et al. 2004, Paper I hereafter) of the new data showed first of all that HD 92024 is an interesting target for asteroseismic analysis: significant, pulsationally driven line-profile variations (LPVs, or 'moving bumps') and, in particular, spectroscopic confirmation of two photometric frequencies. It was, furthermore, the impression that the LPVs were more pronounced than for typical cases of β Cephei stars. The projected rotation rate $v_{\rm rot} \sin i = 75 \pm 20$ km s^{-1} was smaller than the reported literature value (122 km s^{-1}, Balona 1975). By introducing a procedure based on matched-spectrum RV differences, cross correlations using the region $\lambda\lambda$ 4209–4733 provided RV differences which were used to evaluate the orbital parameters with minimum influence by LPVs. The efficiency of this procedure is evaluated in the present paper.

In Paper I, the first combined spectroscopic and photometric analysis of HD 92024 was presented, with the resulting parameters for the respective stellar components: masses of $15.0 \pm 3.0\,\mathrm{M}_\odot$ and $3.0 \pm 0.5\,\mathrm{M}_\odot$ ($q = 0.205 \pm 0.019$), and radii $8.4 \pm 0.8\,\mathrm{R}_\odot$, $2.1 \pm 0.4\,\mathrm{R}_\odot$. The effective temperatures are $25\,500 \pm 500$ K (spectroscopically) and $12\,500 \pm 1000$ K (from the light curve). Surface gravities of $\log g = 3.77 \pm 0.08$ and 4.27 ± 0.18 indicated that the binary consists of an evolved early-B type primary and a late-B main sequence companion. The resulting distance 2.8 ± 0.3 kpc and systemic velocity -16 km s^{-1} confirmed membership of the open cluster NGC 3293, a cluster rich in early-type OB stars including several β Cephei stars. Theoretical stellar models indicated an age of $10 - 13$ Myr. An inclination $i = 85\overset{\circ}{.}2 \pm 1\overset{\circ}{.}7$ was found.

The β Cephei stars are for the moment one of the most successful types of variables to apply in asteroseismological tests, and good agreement between models and observations are found. Therefore, stringent constraints on stellar parameters as derived from eclipsing binaries are most valuable for a better asteroseismological interpretation. In a subsequent Paper II a thorough pulsational analysis based on the available spectra and a larger set of photometric data will be presented.

This paper presents the spectroscopic data in electronic form with final reduced spectra, and a line atlas for a combined high-S/N spectrum of HD 92024 (Appendices A.5 and B). In Sect. 2 the observations and the analysis of the spectra are described, followed by a brief summary in Sect. 3 of the photometry used for ephemeris and frequency analysis in Paper I. Parts of the spectroscopic analysis are then detailed with tests in Sect. 4. In Sect. 5 we summarise and conclude.

2 Observations and data reduction

The observations cover spectroscopy and photometry (CCD and PMT) obtained over the last four years, supplemented with spectra more than a decade old. All data were obtained at the ESO La Silla observatory. In addition, photometric data from the literature were included.

The complete set of spectra is listed in the observing log in Table 3 in Paper I, and comprises 9 recent nights on the FEROS spectrograph and 5 nights with ECHELEC in 1989. We obtained 103 high-resolution spectra with the FEROS echelle spectrograph during two periods, February–March 2001 and February 2002. FEROS is a fibre-fed (object+sky) spectrograph which provides a resolution $R = 48\,000$ and a wavelength range of $\lambda\lambda\,3700$–8600, and is equipped with a thinned and backside-illuminated 2k $\times$ 4k EEV CCD.

During five nights in February 1989, 23 spectra were obtained with the ECHELEC spectrograph, covering the range $\lambda\lambda\,4390$–4715. ECHELEC is a Littrow echelle spectrograph having a grism as cross disperser, a resolution $R \sim 25\,000$, and a thinned back-illuminated RCA CCD with 1024$\times$640 pixels. All the FEROS and ECHELEC spectra were obtained at the ESO 1.52-m telescope.

2.1 Echelle spectroscopy

The main purpose of the analysis of the spectra will be the study of the line variability due to pulsations (Paper II), although the first application was the determination of the spectroscopic orbital parameters (Paper I). Both types of projects profit largely from the reduction of noise by inclusion of all relevant spectral features. In a rotationally-broadened early-type spectrum, consistency between different spectral features depends sensibly on the normalisation of the spectra, and in particular on the removal of the echelle blaze modulation of the intensities in the many spectral orders. This modulation is, in general, time-dependent. The FEROS pipeline, very useful for first-look purposes, is not intended to provide this consistency. We therefore improved the data reduction with as main concern the consistent removal of time-dependent factors to below the 1% level in the normalisation procedures. However, many details of the whole data reduction procedure were finally altered, as summarised in the report by Hensberge (2001). The most important changes are shortly summarised here.

Most importantly, the FEROS spectra are reduced differentially relative to a 'master' stellar and flat-field frame, and the spectral orders are merged only after time variation in the blaze function, instrument response (changes in light path) and sky transparency have been taken out. It was found, not only for this fiber spectrograph, that especially the calibration unit introduces time-dependent blaze-function characteristics (Skoda & Hensberge, 2003). A disturbing property of the flat-field calibration spectra was e.g. the presence in the 2001 spectra of an undulating intensity component in the 4800–6200 Å range, with a maximum range of 5% in intensity and a time-variable phase. The effect is absent in science and dome flat-fields. In 2002, the range was at least an order of magnitude smaller. Less disturbing, but still relevant, is an apparently variable vignetting at the extremes of the spectral orders, especially at the lower wavelength side. This effect occurs in all types of exposures and contributes to imperfect overlap of the spectral orders. Taking shorter overlaps than one would do on the basis of random-noise arguments reduces the problem significantly, but nevertheless the effect was studied in detail and remedied further as explained below. We suspect that the latter vignetting effect is due to malfunctioning of the shutter unit, as the vignetting effect at one point grew to unacceptable levels when the shutter unit had serious problems.

Time-dependent effects related to the calibration unit were removed from the extracted frames before flat-fielding the science exposures. The term 'removed' should be understood in the sense that the instrumental bias would be, after the applied correction, identical in all calibration frames. In 2002, this was done using an appropriate robust 2D-model for the ratio of each lamp flat-field relative to a master flat-field. In 2001, an additional step was necessary: removal of the time-dependent undulating function in the master lamp flat-field using dome flat-fields. The vignetting effects present in all types of exposures were mapped separately for the flat-field and science frames, again by a 2D low-frequency model for the ratio of the intensities in an individual frame relative to the extracted master (flat-field or science) frame. This model

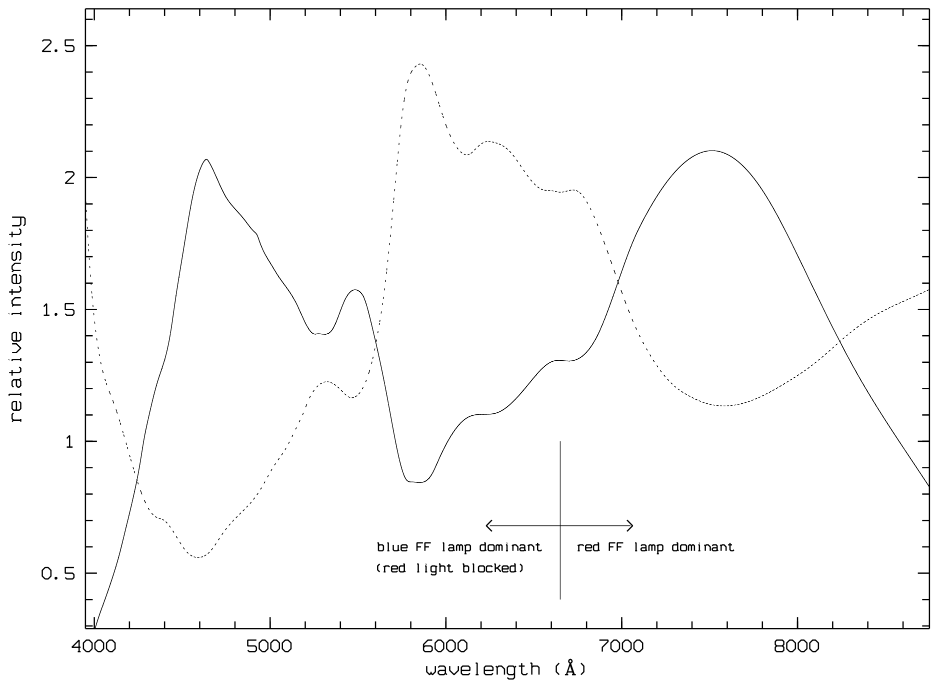

Figure 1: Dashed line: ratio of dome and calibration lamp flat-field, including a first-order correction for a colour-temperature difference. Note the wiggles in the intensity distribution caused by the combination of filters used to block the red light of one of the calibration lamps. Full line: fitted global intensity distribution of the flat-field calibration lamps. As an initial step in the normalisation procedure, flat-fielded science spectra are multiplied with this function.

consists of the product of two factors: a low-order bivariate polynomial in the coordinates (pixel along order, order number) multiplied by a smooth spline function that does not depend on the order number. Several aspects of the time-dependent blaze-function, end-of-order vignetting and applied models are discussed and graphically represented in Hensberge (2004).

Since the science exposures and the flat-field exposures are thereafter on the low-frequency level perfectly consistent with each other before the spectral orders are merged, all merged spectra can be normalised using the same one-dimensional function: the modification of the intensity of the lamp flat-field by the filters in the calibration unit is derived directly from comparison of calibration lamp flat-fields with dome flats (Fig. 1, full line) and separated from the other causes. The latter are modelled on the merged master science frame, as usual, iteratively identifying (pseudo)-continuum windows. This procedure guarantees a high level of consistency between the normalised spectra, with normalisation errors below the one percent level everywhere – except for the 4150–4200 Å region that is severely disturbed by two consecutive hot columns.

The intervals selected in each spectral order to contribute to the merged spectra are listed in Table 1. In general, the useful part of an order is selected from considerations of random noise and of uncertainties related to the division by the blaze function. Additional constraints are that subsequent spectral orders should have an overlapping wavelength range exceeding the full width of a typical spectral line, and that the spectral overlap of subsequent orders should be consistent. The latter is obtained through small shifts (< 10 pix) of the blaze profile along the order. Finally, the need to avoid non-linear columns of the detector overruled the previous considerations in a few cases.

Moreover, some of our other reduction algorithms differ from the standard ones:

- location of the orders (i) using *all* unblemished cross-cuts in the parts of the spectral orders that will be used effectively in the merged spectra, (ii) taking discretisation effects out of the centring algorithm and (iii) applying a robust two-dimensional model. Leaving out the 'ends' of the spectral orders (in fact, very short parts remain in the bluer orders) from the fit, prevents that noisy and biased information would influence the final order location model in the parts defining the final, merged spectrum. The resulting rms deviations from the measured positions relative to the 2D model are then 0.01 pix in the well-exposed orders of flat-field images (they would be at least a factor of 5 higher without removal of discretisation effects), and somewhat larger in less-exposed orders, including stellar images, fully in accord with the expectations for increased random noise in the data;

- background modelling taking into consideration overlap of close spectral orders in the redder part of the spectrum;

- linear extraction and a different cosmic ray detection strategy. Optimal extraction and straightforward cosmic ray detection fails due to the presence of an image slicer at the exit of the fibres, producing two overlapping images shifted several tenths of a pixel in the wavelength direction with respect to the detector rows;

- robust 2D-wavelength calibration with a ThAr+Ne lamp (absolute calibration for one master lamp spectrum, differential calibration of the other lamp spectra) followed by the use of telluric line positions to monitor zero-point shifts between different observing runs as well as rapid,

Table 1: Notes and remarks on the FEROS order merging. Start and end points are indicated for each spectral order (Col. 1), and remarks are given on non-linearities and used overlap regions. Brackets refer specifically to the 2001-spectra when orders were cut at a different place than for the 2002 data. '*' indicates wavelengths selected by considering the detector's non-linearity rather than the random noise and blaze modulation error propagation. Note that the non-linearity positions are for the object fibre only.

Ord. #	$\lambda_{\rm start}$ (Å)	$\lambda_{\rm end}$ (Å)	Remarks and action taken
63	3568.85	3630.00	order extraction dubious
62	3626.00	3690.00	
61	3686.00	3752.00	
60	3748.00	3820.00	
59	3816.00	3889.00	
58	3885.00	3954.00	
57	3950.00	4024.00	
56	4019.00	4096.00	
55	4089.00	4178.00	$\lambda > 4149$ non-linear
54	4178.00*	4245.00	$\lambda < 4202$ highly non-linear detector col. 1299+1300
53	4236.00	4334.00	$\lambda\lambda 4309 - 4317$ taken from sp. ord. #52
52	4323.00	4408.00*	end-point to avoid detector col. 1299+1300
51	4400.00	4496.00*	end-point to avoid detector col. 1299+1300
50	4485.00	4584.00	
49	4574.00	4683.00	$\lambda\lambda 4663 - 4665$ slightly non-linear
48	4672.00	4785.00	
47	4774.00	4888.00	$\lambda\lambda 4862 - 4873$ taken from sp. ord. #46
46	4862.00*	4981.00*	end-point to avoid detector col. 965
45	4976.00	5102.00*	end-point to avoid detector col. 965
44	5092.00	5220.00	
43	5205.00	5341.00	$\lambda > 5316$ slightly non-linear sections
42	5326.00	5469.00	
41	5452.00	5600.00	
40	5582.00	5748.00	
39	5728.00	5890.00	
38	5870.00	6047.40	
37	6027.40	6210.00	
36	6189.50 (6185.00)	6385.00	
35	6365.80 (6360.00)	6577.00*	end-point to avoid dark detector col. 327 in sp. ord. #34
34	6570.00*	6758.00	start-point to avoid dark detector col. 327
33	6749.68 (6742.77)	6968.00	$\lambda\lambda 6887 - 6905$ non-linear
32	6957.75 (6953.31)	7185.00	$\lambda\lambda 7128 - 7145$ non-linear
31	7170.19 (7172.70)	7420.00	$\lambda\lambda 7378 - 7392$ non-linear
30	7416.14 (7414.00)	7672.00	$\lambda\lambda 7642 - 7652$ non-linear
29	7669.36 (7658.00)	7932.10	$\lambda > 7921$ non-linear
28	7932.00	8226.10	$\lambda > 8218$ non-linear
27	8226.00	8533.00	inter-order gap #27 / #26
26	8542.00	8860.00	inter-order gap #26 / #25
25	8886.00	9214.00	order extraction dubious

cyclic wavelength shifts due to improper temperature control in the spectrograph room at the 1.52-m telescope. The rapid shifts amounted to 0.6–0.8 $\mathrm{km\,s^{-1}}$ over 30–40 minutes around a stable average. Presently, at the 2.2-m telescope, this problem has been remedied and wavelength stability is now excellent (0.04 $\mathrm{km\,s^{-1}}$ rms).

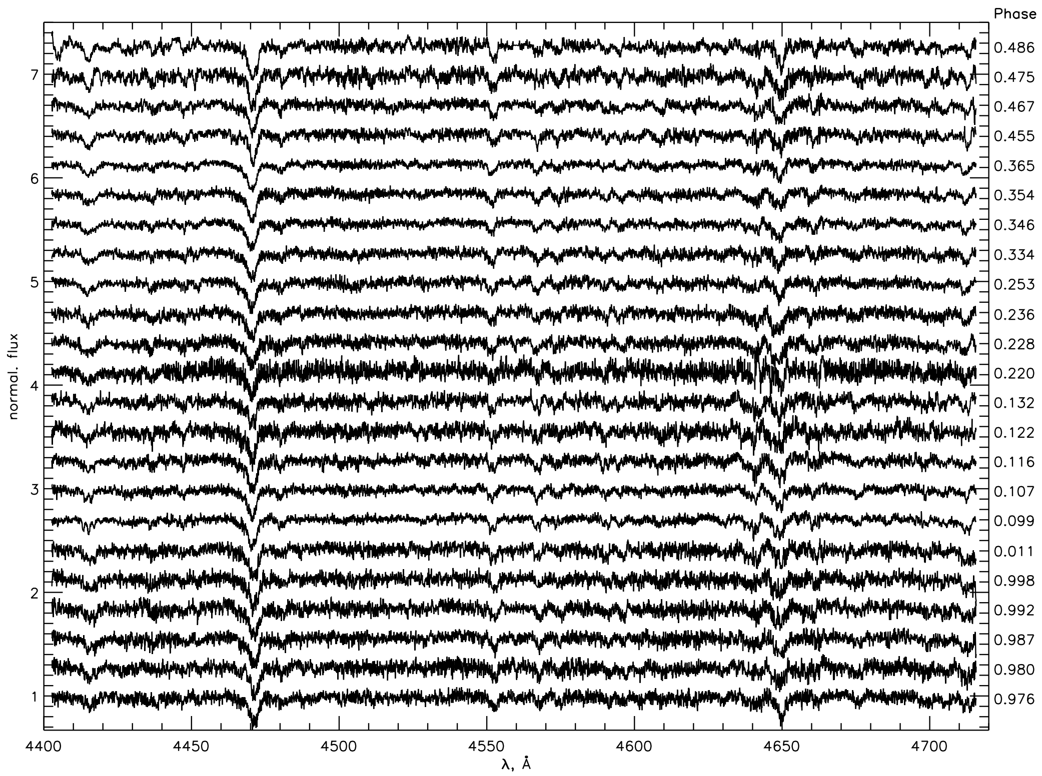

Figure 2: The final ECHELEC spectra with orbital phases indicated (right-hand side). Subsequent individual spectra are separated along the vertical axis by 0.29 (100% absorption is 1 unit).

Note that the spectra are rebinned only once while also taking into account the barycentric velocity correction, to avoid unnecessary correlation of noise. They are rebinned in $\ln\lambda$, rather than wavelength, for two reasons: to better conserve the natural resolution on the detector (the pixel size expressed in $\mathrm{km\,s^{-1}}$ varies less than 1% around 2.727 $\mathrm{km\,s^{-1}}$ over all spectral orders), and to anticipate the cross-correlation velocity analysis.

The spectra from the sky-fiber are available, but were presently not used and therefore not examined in the same detail as the stellar spectra for blemishes. To remove the most obvious (cosmic ray) blemishes from the sky spectra, a simple semi-automatic routine was applied. Note that the wavelength positions of the non-linear detector sections given in Table 1 do not apply to the sky spectra. When removing the sky fiber signal from the stellar spectrum, it should be taken into account that the efficiency of the sky fiber is only 60% of the efficiency of the stellar fiber (as measured from dome flat-fields during the 2002 observing run). This ratio is almost wavelength-independent.

In view of the more limited quality of the ECHELEC spectra (long integration times, low S/N and small wavelength coverage), we did not make the effort of performing a dedicated reduction procedure. Known shortcomings of the applied standard reduction procedure (see Verschueren et al. 1997 for details), performed with the available MIDAS routines shortly after the observations, were partially remedied using *a posteriori* corrections. The ECHELEC spectra suffer from three adjacent hot columns affecting relatively short wavelength regions in three consecutive spectral orders, and from improper order merging. We used our experience with the masking of these columns in another research project with the same instrument to take out most of these adverse effects, assuming that the non-linear columns producing intensity-independent (within the exposure range of the different spectra) and time-independent static bias in the spectra. Such assumption proved sufficient to reduce the spurious features by an order of magnitude to the level of the photon noise on individual pixels in these spectra. Improper order merging was improved by a "re-normalisation" of the spectra using the less noisy and well-normalised FEROS spectra as templates. These limitations imply that the uncertainties on derived spectral quantities are larger than in the case of purely random noise. For example, in an averaged spectrum systematic noise clearly dominates over random noise.

2.2 Photometric observations

Table 2: Photometric indices and data for HD 92024 (P) and comparison stars. Sources: Kaltcheva (2003) and Shobbrook (1983) (C1)

ID	Type	$\alpha_{2000.0}$ hh:mm:ss	$\delta_{2000.0}$ °:′:″	V mag	$b-y$ mag	m_1 mag	c_1 mag	β mag
P	B1III	10:36:08	–58:13:05	9.024	0.034	0.040	0.011	2.605
C1	B1III	10:35:58	–58:13:22	8.038	0.085	0.010	–0.014	2.577
C2	B5V	10:36:33	–59:11:25	7.094	–0.038	0.100	0.428	2.709
C3	B5III	10:32:21	–58:32:45	7.365	–0.026	0.081	0.371	2.693

The photometric data will be presented in a future data paper following Paper II, and will include all measurements and details on calibration.

Summarising from Paper I, 1126 Strömgren *uvby* photomultiplier (PMT) data points were obtained with the 0.5-m Strömgren Automatic Telescope

(SAT) during 15 nights in the course of Dec 2002–Apr 2003. The observations were done continuously, differential to the comparison stars in Table 2, around and in the eclipses. Evaluation of rms for the difference light curves of the comparison stars showed constancy down to the level of 6 mmag. A second test with frequency analysis with `Period98` (Sperl 1998) for 421 points with C2 and C3 as comparison stars for C1, rejected cyclic variability above the 3 mmag-level in the frequency range 0–50 $\mathrm{c\,d^{-1}}$. Based on this we used all three comparison stars in the differential HD 92024 photometry.

In addition, we added two hours of CCD observations obtained in Apr 2001 using the Danish 1.54-m telescope with DFOSC (2k × 2k LORAL-LESSER CCD, $0.''40$ $\mathrm{pix^{-1}}$). From other CCD data, obtained as part of the Long-Term Photometry of Variables (LTPV) project (Sterken 1983), a subset from the Dutch 0.9-m, La Silla and the 1-m, Sutherland, SAAO, South Africa was extracted for measurements around times of light minimum aimed at improving the ephemeris of HD 92024. Unfortunately the extracted sequences of images were too short, compared to the pulsation cycles of HD 92024, which made it difficult to bring the photometry on the same scale and prewhiten the pulsation frequencies. These data were, however, fully compatible with the refined ephemeris given in Eq. 1, but since they added noise rather than reducing it, they were saved for the pulsational analysis in Paper II where all out-of-eclipse data will be included.

The Danish 1.5-m CCD and the SAT PMT data were then combined with photometry published by Engelbrecht & Balona (1986, B CCD-data) and JS92 ($b, uvby$ PMT-data) by adding magnitude offsets determined from available out-of-eclipse observations; for improving the ephemeris, a comprehensive *blue* light curve was made by combining all B and b data (2277 points), while for the binary model analysis a set with simultaneous $uvby$ observations was composed (1671 points in $uvby$ + 20 in b alone).

3 Photometric data

The light variability in HD 92024 caused by the primary's pulsations was removed from the light curve using the following procedure: 1468 out-of-eclipse data points were selected from the *blue* data set; by calculating power spectra (Fig. 3) with `Period98` we sequentially searched for and removed the three most significant frequencies in the light curve. The adopted frequency solution was $f_1 = 5.6400$ $\mathrm{c\,d^{-1}}$, $f_2 = 6.6613$ $\mathrm{c\,d^{-1}}$, $f_3 = 7.1624$ $\mathrm{c\,d^{-1}}$ and corresponding semi-amplitudes $a_1 = 7.4$ mmag, $a_2 = 3.8$ mmag, $a_3 = 4.2$ mmag. The scatter of this solution is $\sigma = 6.8$ mmag, as seen in the phase diagrams of Fig. 4 for the light curve phased with each frequency, having the other fre-

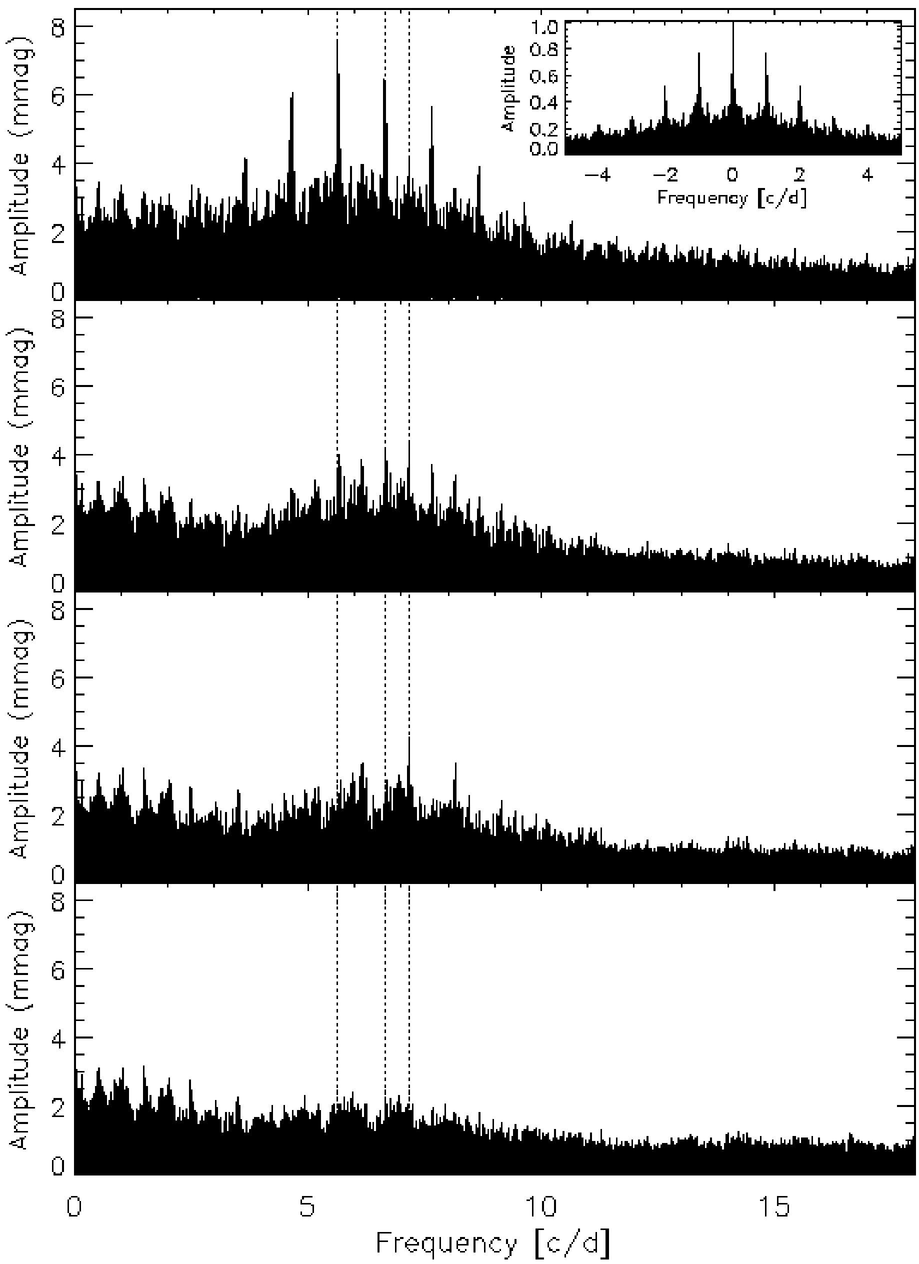

Figure 3: Amplitude spectra showing significance of the frequencies that were used to prewhiten the light curves. Successive prewhitening for $f_1 = 5.6400$, $f_2 = 6.6613$ and $f_3 = 7.1624$ c d^{-1} follows from top to bottom. Out-of-eclipse data were used. Dotted lines indicate positions of f_1, f_2, f_3. In the upper panel the window function is inserted.

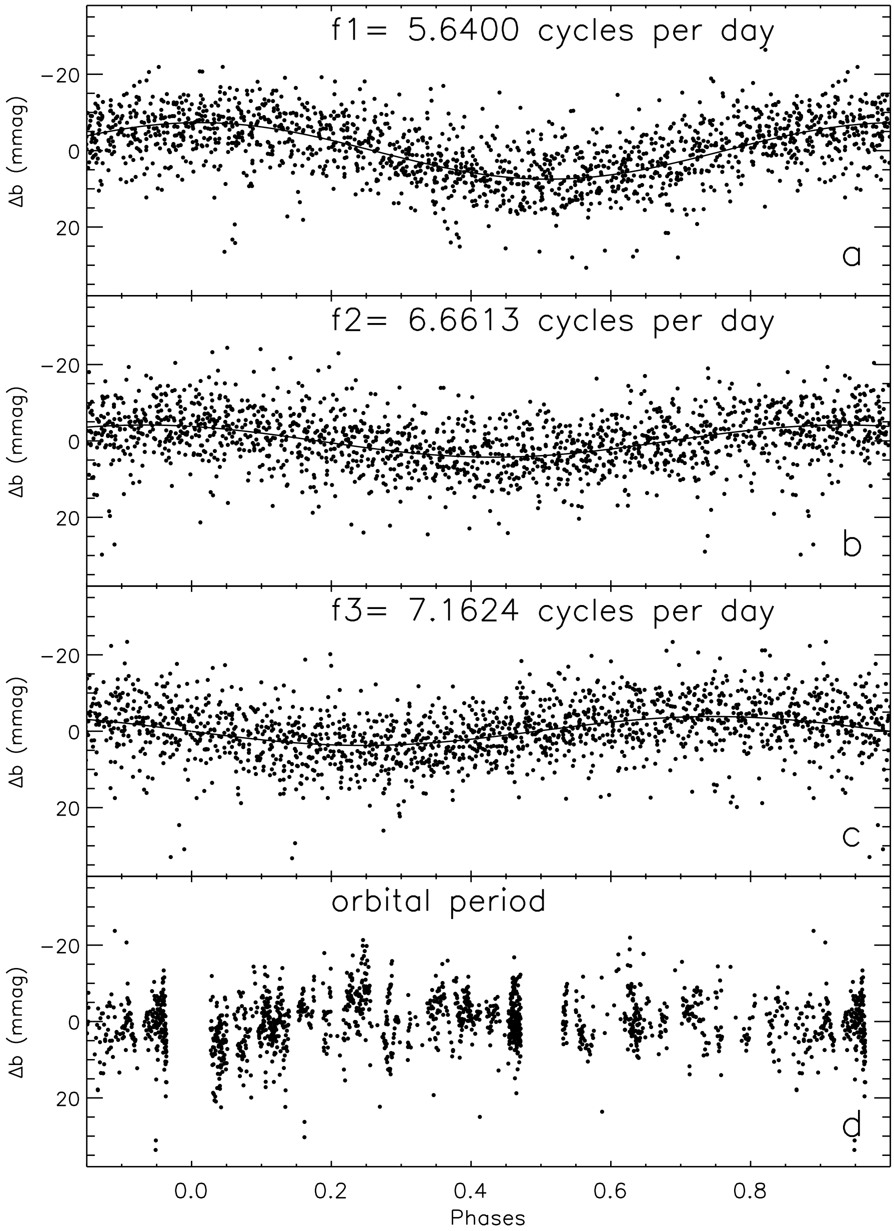

Figure 4: Phase diagrams for the same light curve and frequencies as in Fig. 3. Panels **a** to **c** show the phased light curve for resp. f_1, f_2 and f_3, in each case with the two other frequencies prewhitened. Panel **d** illustrates the noise level in the residual light curve, phased with the orbital period. The two gaps are due to the exclusion of the eclipses. Sinusoidal models are superimposed with thin lines.

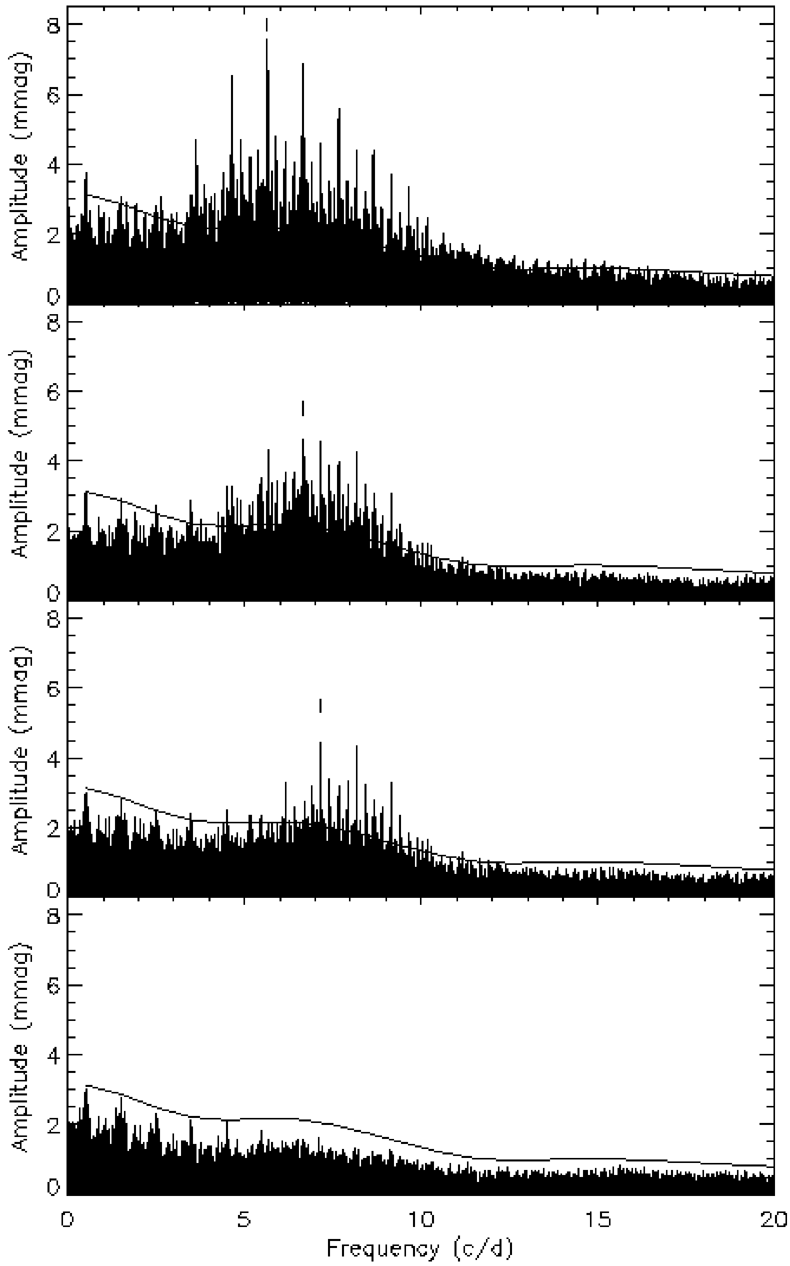

Figure 5: Fourier amplitude spectrum of the b light curve after removal of the model light curve from Paper I. Identifications (marked with a vertical bar) and successive prewhitening of f_1, f_2, f_3 follows from top to bottom panel. The 4σ significance level is indicated.

quencies prewhitened. The *uvby* light curves were then prewhitened for the frequencies in this solution. The detected frequencies are the same as found by Engelbrecht (1986), but low-amplitude systematic variability remains in the light curves after prewhitening. Thus the frequency solution probably still is incomplete but the residuals no longer critically obstruct the photometric analysis in Paper I.

We are convinced of the three frequencies for the following reasons:

1. through a frequency analysis using only a sub-sample of the light curves all three frequencies are still detected;

2. the frequencies nicely reproduce *uvby* light curves from two additional nights of SAT photometry obtained in 2004;

3. a check on the frequencies using the full b light curve corrected for the orbital model of Paper I strengthens the evidence: as seen in the subsequent detection and removal of frequencies in Fig. 5, we get similar power spectra, with all three frequencies clearly detected above the 4σ significance level (superimposed near-horizontal line in the Figure): $f = 5.6406$ (6.6 mmag amplitude), 6.6584 (4.9 mmag), and 7.1624 $\mathrm{c\,d^{-1}}$ (5.0 mmag) (1690 data points, $\sigma = 0.0054$ mmag). The smaller scatter of this solution, compared to the one used for prewhitening the light curves, is due to the removal of binary-induced out-of-eclipse variations (stellar reflection effects, mostly) clearly seen in the lower panel of Fig. 4.

We emphasise that the f_1, f_2, f_3 solution is preliminary for the following reasons: f_2,f_3 just exactly fulfil the 4σ detection criterion commonly used (see e.g. Freyhammer et al. 2001); aliases could alter them and more frequencies may be present. The exact frequencies should be confirmed with a larger set of photometry corrected for eclipse variations. We do, however, emphasise that f_3 (or one of its aliases) can be considered certain as it is a clear detection in the spectroscopy (Sect. 4.2).

A refined ephemeris was calculated from the *blue* light curve. Because the duration of a complete eclipse surpasses the length of an observing night, the full light curve was analysed using the procedure by Lafler & Kinman (1965). From a fine grid of test periods centred on the period by JS92, minimum θ was searched for. For $8\overset{\mathrm{d}}{.}324565$ we find a minimum θ for the current sampling (Fig. 6), and taking the scatter into account we determine an improved orbital period $8\overset{\mathrm{d}}{.}32457 \pm 0.00002$.

Then, using the method of Kwee & van Woerden (1956) on the data in primary eclipse, also the time of mid-eclipse was improved: HJD 2 445 391.4030 ±

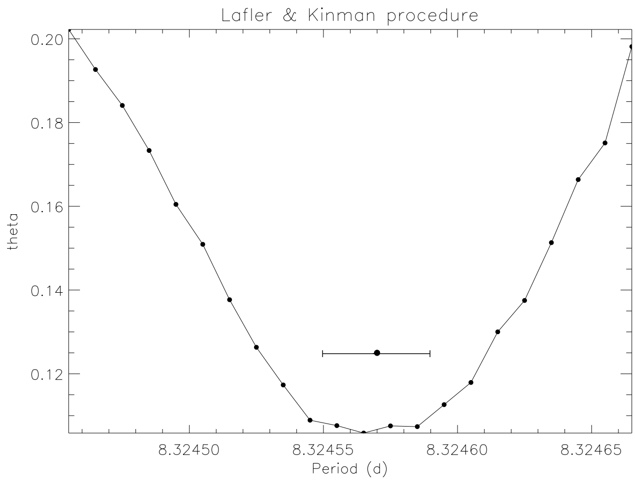

Figure 6: The variation of θ (Lafler & Kinman 1965) around its minimum using the *blue* light curve (2263 data points). Minimum *theta* with uncertainty is indicated by the dot and horizontal bar. The small dots indicate the test periods.

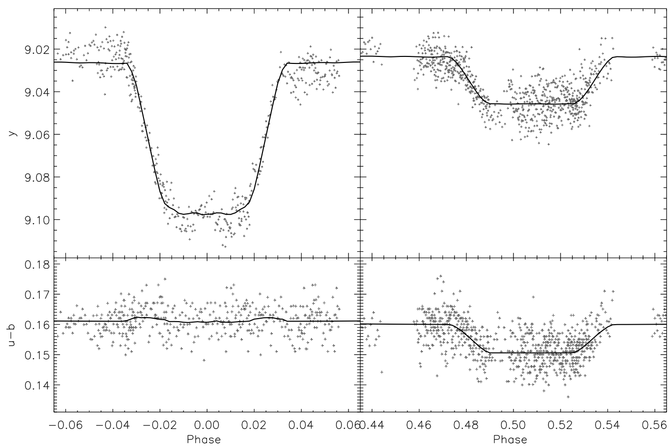

Figure 7: The eclipses in the b light- and $u - b$ colour-curves prewhitened for pulsational frequencies. The binary model light curve from Paper I is superimposed.

0.0008. The refined ephemeris for primary light minimum is:

$$\begin{array}{rll} \text{Primary Min} = \text{HJD } 2\,445\,391.4030 + & 8\overset{\text{d}}{.}32457 \text{ E} \\ \pm 0.0008 & \pm 0.00002 \end{array} \qquad (1)$$

The improved values are within the error bars of JS92's ephemeris but more accurate. The phase of secondary mid-eclipse is $0\overset{\text{p}}{.}507 \pm 0.001$, indicating a

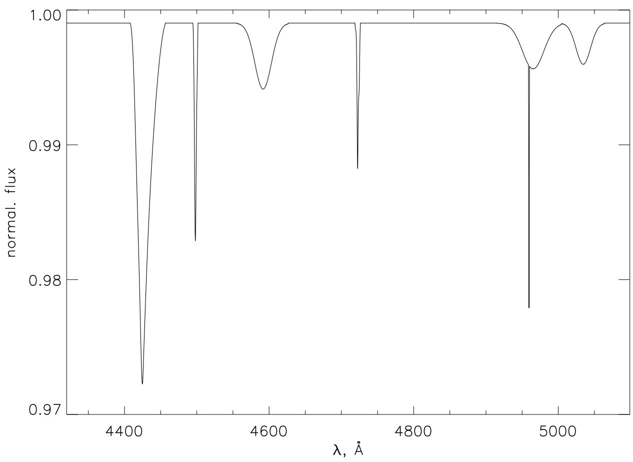

Figure 8: Model of significant DIBs eliminated in the FEROS spectra.

small but significant eccentricity, as seen in Fig. 7. In this figure, a zoom-in on the two eclipses is shown for the b-light and $u-b$ colour curves with the binary model light curve (from Paper I) superimposed. The centre of the secondary minimum is positioned later than a half-period after the primary minimum, which indicates eccentricity. For the SAT data alone, the required change in orbital period to reposition the minima such that the circular case is obtained would be far beyond the accuracy on the period itself. Eccentricity is therefore required. Tests excluded measurable apsidal motion during the 19 yrs spanned by the *blue* light curve.

4 Spectroscopic analysis

In the cross-correlation analysis of the spectra, presence of any significant static, or non-stellar, feature (blemishes, telluric line emission, diffuse interstellar bands or DIBs, etc.) would have an adverse effect and were therefore eliminated on forehand.

Superimposed on the stellar spectra is a number of emission lines from the surrounding H II region and the Earth atmosphere. Some of the most significant lines were identified with the catalogue by Meinel et al. (1969) as indicated in Table 3. These lines do not affect the cross correlations in the wavelength regions we selected and were, therefore, not removed, although this option exists using the sky fibre spectra.

A line atlas was made for HD 92024 (Appendix B) by combining the stellar FEROS spectra after adding velocity shifts to remove the orbital shifts. The

Table 3: The most significant emission lines in the FEROS spectra.

$\lambda_{\rm lab.}$	Line ID	$\lambda_{\rm lab.}$	Line ID
4861.3 Å	H II region	7794.0 Å	OH air glow
5577.4 Å	O I air glow	8399.3 Å	OH air glow
6300.2 Å	O I air glow	8430.2 Å	OH air glow
6363.9 Å	O I air glow	8465.2 Å	OH air glow
6562.8 Å	H II region	8465.6 Å	OH air glow

non-stellar emission lines (we find no stellar emission) are, therefore, smeared by four groups of velocity shifts –35, –8, 22, 46 $\mathrm{km\,s^{-1}}$ (see Fig. 13), imposed by the orbital phases covered, but could instead be studied by combining the sky-fiber spectra. The only emission from the nebula is seen in Hα (strong) and Hβ (faint). At shorter wavelengths O I air glow dominates the emission lines, while further in the red OH emission dominates.

Moreover, the FEROS spectra were inspected, interactively as well as with an automated procedure, in order to detect and remove quasi-static features due to bad pixels and other blemishes, and remaining effects from cosmic rays. DIBs around $\lambda\lambda$ 4429, 4502, 4595, 4727, 4964, 4970, 5039 contribute with up to 3% absorption of the continuum and were unblended enough to be modelled (Fig. 8) and divided out of the spectra, guided by the list of Jenniskens & Désert (1994). The spectra included in Appendix A.2 were not subtracted by this DIB model. In some cases, such as near to Hβ, it was not possible to properly model and eliminate significant DIBs.

The FEROS spectra reveal substantial line-profile variations (LPVs), as illustrated in Fig. 11 for Si III λ 4553, in spite of the substantial integrations of 20 minutes required for having $S/N = 100$, smearing out LPVs during one tenth of the pulsational cycle. Within 70 $\mathrm{km\,s^{-1}}$ from the centre of the line, the local line depth of many lines changes more than a factor of 2 during a pulsation cycle while producing variable subcomponent line-structure. These variations seem more profound than typically reported in the literature for several other β Cephei stars.

4.1 A high-S/N template

As an aid in the spectroscopic analysis, and for having a template to cross-correlate all spectra for comparative purposes, we constructed a '103-spectrum composite', made by averaging all FEROS spectra with orbital shifts eliminated, using the orbital model of Paper I (Table 6, this paper). These model-predicted orbital velocity shifts are listed in a digital table included as file `RVSHIFTS.DAT`. Having $S/N \approx 1\,000$, this template shows the average line-profile shapes and is valuable for detecting faint lines for the atmosphere analysis and faint blends that may affect the conclusion of a pulsational analysis. Appendix B presents this spectrum composite with line identifications for the full wavelength range. The graphical representation of the average spectrum still includes DIBs (smeared by the removal of orbital motion), as such bands have astrophysical information.

In addition, a 'narrow-line spectrum composite' average of 10 spectra was made. This composite represents an extreme case of deep and narrow line profiles, which we use in Sec. 4.4 in a comparison with spectra of σ Sco.

4.2 Pulsational frequencies

For the purpose of attempting mode identification in Paper II, the pulsational information from photometry and spectroscopy should be combined: photometry provides information on disk-averaged light variability and temperature changes during the pulsations, while spectroscopy provides information on velocity- and to some level temperature variations.

As demonstrated by Schrijvers et al. (2004) power spectra calculated in wavelength bins across a spectroscopic line can be combined to improve the power of oscillation frequencies. We anticipated that this method is even more valuable when having spectra covering a large wavelength range, as there are more lines present to provide pulsational information. Phase and amplitude differences for LPVs in different lines would not affect the corresponding periodograms and they can be summed directly. This was tested in practice on all FEROS spectra, shifted in wavelength to eliminate the orbital shifts. Paper I provided a quick test of the efficiency of combining more regions by summing power spectra over the O II $\lambda4596$ and Si III $\lambda4553$ profiles.

These two lines were selected from a line list based on an evaluation of the pulsational information content in the spectra (Table 4). For each wavelength bin of 2.727 km s^{-1}, the rms of all normalised fluxes relative to their mean was computed ($\sigma_{\rm tot}$) and corrected for random noise, defining $\sigma_{\rm var}$ from $\sigma^2_{\rm tot} = \sigma^2_{\rm var}+\sigma^2_{\rm ran}$. The random noise $\sigma_{\rm ran}$ dominates in the far blue ($\lambda < 3900$ Å) and at wavelengths with little variability (small $\sigma_{\rm var}$) and was estimated from a spline fit to $\sigma_{\rm tot}$ in continuum windows. A better (but more demanding) approach would take into account the changing number of counts with the blaze profile, as well as where the order-overlap reduces random errors in the merged spectrum. Taking $\sigma_{\rm var} \geq 0.015$ as the limit for including bins in the frequency analysis, the FEROS spectra provide us with 27 spectral lines (Table 4), with valuable pulsational frequency information. The largest $\sigma_{\rm var}$ scatter encountered at any wavelength is 0.03. The detailed analysis of this information, not only in terms of pulsation frequencies, but also in terms of amplitudes and

Table 4: List of 27 spectral features with significant variation due to pulsations. The lines indicated (Cols. 2 and 5) are the main contributors in the respective regions. The $\sigma_{\rm var}$ column is in units of normalised flux.

Region Å	line(s)	$\sigma_{\rm var}$ flux	Region Å	line(s)	$\sigma_{\rm var}$ flux
4024.9–4026.9	He I	0.017	4565.4–4569.4	Si III	0.023
4067.8–4070.5	O II - C III blend	0.021	4572.7–4575.9	Si III	0.016
4070.8–4072.9	O II	0.015	4589.3–4592.2	O II	0.015
4074.6–4076.5	O II	0.020	4594.1–4597.1	O II	0.015
4087.2–4090.3	Si IV + O II	0.017	4637.0–4643.4	O II + N II + N III	0.016
4117.3–4121.8	He I + O II	0.021	4645.6–4652.0	O II + C III	0.026
4251.8–4257.0	O II	0.015	4659.3–4663.0	O II	0.018
4265.4–4268.3	C II doublet	0.017	4710.9–4714.5	He I	0.022
4343.8–4352.5	O II (4 lines)	0.024	4919.7–4923.0+	He I	0.023
4386.2–4388.9	He I	0.018	5013.2–5017.2	He I	0.022
4413.1–4417.8	O II + O II	0.024	5046.2–5048.7	He I(+ N II)	0.015
4469.5–4472.4	He I	0.024	5872.7–5877.9	He I	0.031
4479.6–4482.2	Mg II (+ Al III)	0.016	6674.9–6680.2	He I	0.029
4550.5–4554.0	Si III (+ N II)	0.026			

phases throughout the line profiles, will be a subject of Paper II. We emphasise that the $\sigma_{\rm var}$ variability index does not scale strictly with line strength – compare e.g. He I λ4713 with the twice deeper line He I λ4388 (Table 4 and the spectral atlas, Appendix B) – and that line blending can significantly counteract spectral variability, depending on the wavelength separation between the components. Like this, the $\sigma_{\rm var}$ parameter is useful for comparison of the level of the spectral variability for lines of different strengths and over the line profile itself.

Currently, only Si III 4553 and O II 4596 were selected and evaluated by computing power spectra with `Period98`, for bins corresponding to 5.5 km s^{-1} and 70.9 km s^{-1} in size. The corresponding $\sigma_{\rm var}$-scatter spectrum for the region λλ=4548–4602 is shown in Fig. 9 (top panel).

For comparison, the lower panel shows the 103-spectrum composite. These two lines are (nearly) unblended: the Si III is very strongly variable, the O II only moderately so. In particular they are two different species so the LPVs may behave differently.

With only 103 spectra, obtained during two short periods of 4–12 days duration, separated by one year, strong aliases for 1, 1/11, 1/350 c d^{-1} are unavoidable in the Fourier analysis (see e.g. the corresponding window function in the top panels in Fig. 10). For the summed (5.5 km s^{-1} bin) power spectrum, two of the three photometric frequencies (Sect. 3) are prominent

(Table 5, Cols. 6–7) and contrary to the photometry, f_3 has highest power in the spectroscopy, while f_1 is ambiguous. Due to the complicated window function, several close frequencies are equally valid to f_3 and f_2: $f_3 = 7.1622$ and 7.1680 c d^{-1} (amplitudes = 0.0171), $f_2 = 6.6649$ and 6.6591 c d^{-1} (amplitudes = 0.0106).

The noise level of the summed power spectrum is more than a factor of two lower than is the case for two power spectra with single 70.9 km s^{-1} bins per Si- or O-line profile (Fig. 10). A bin width of 70.9 km s^{-1}, or 1 Å, represents the width of the line cores (more precisely we used 4551.67–4552.74 Å and 4595.08–4596.15 Å), but because of the wavelength dependence of the spectral line variability, even that width introduces some of the scatter seen in the figure. For wider bins the increase in noise in the periodograms becomes especially strong. Columns 2–5 in Table 5 give the detected frequencies in the two 70.9 km s^{-1} bin periodograms. For comparison, the corresponding result of the summed power spectrum (summed over all 5.5 km s^{-1} bins in 1.5 Å of the two line cores) is included in Cols. 6–7. Only f_3 and f_2 are detected on the 4σ-significance level and with a considerable uncertainty of which alias peak corresponds to the true frequency; various unlisted alias frequencies have similar power. The frequencies are given with three significant digits only, again because of multiple close alternative frequencies due to the complex shape of the window function (Fig. 10) which shows more close aliasing frequencies with similar power. An example is the frequencies from the Si-line region in Table 5: $f_3 = 7.159, 7.156$ or 7.162 c d^{-1} are equally good choices, while $f_2 = 6.659$ c d^{-1} is slightly more significant than the 6.656, 6.662, 6.665 alias peaks. A third frequency $f = 5.228, 5.231, 5.233$ or 5.225 c d^{-1} is on the limit of detection, mostly depending on the selected size of bin width.

Table 5: The frequencies f_3 and f_2 as found in two power spectra for the flux integrated over Si III 4553 and O II 4596 (Cols. 2–3, 4–5 resp., cf. Fig. 10) and the summed power spectrum, summed over all bins over both line cores (Cols. 6–7). The frequencies are numbered as in the light-curve analysis. Amplitudes are in units of normalised flux, frequencies are given in c d^{-1}.

	Si III 4553		O II 4596		Summed Power spectrum	
	Freq.	amplitude	Freq.	amplitude	Freq.	amplitude
f_3	7.159	0.0135	7.151	0.0099	7.1651	0.0172
f_2	6.659	0.0096	6.665	0.0058	6.6620	0.0106

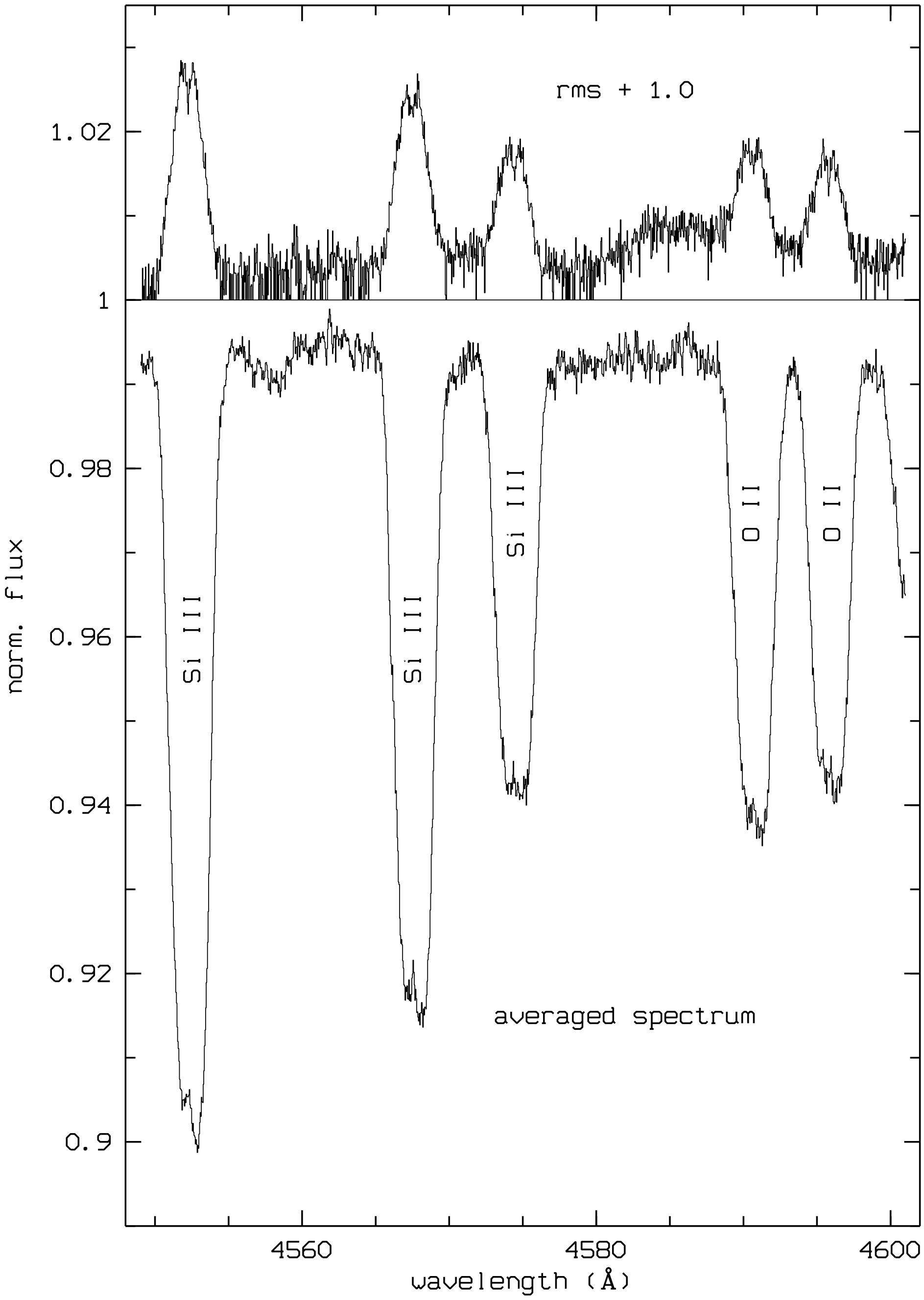

Figure 9: Selection of spectral lines with pulsational information. Top: rms over the 103 FEROS spectra after taking into account the local random noise $\sigma_{\rm ran} = 0.0087$, showing the scatter $\sigma_{\rm var}$ due to the LPVs (shifted by adding 1). Bottom: the corresponding part of the 103-spectrum composite, including the lines Si III λ4553 and O II λ4596 selected for the frequency analysis.

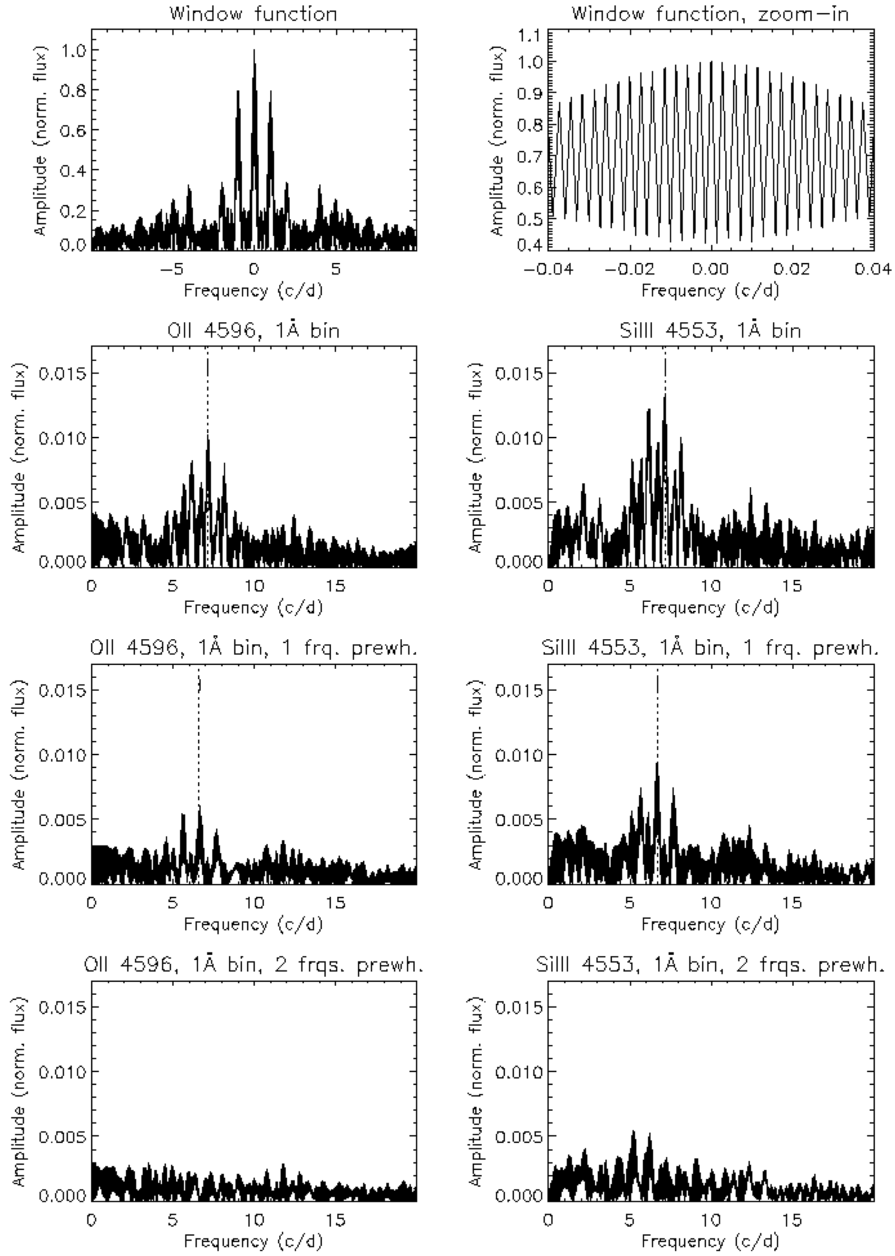

Figure 10: Power spectra for the O II 4596 (left) and Si III 4553 lines (right) using only a single bin corresponding to a width of 70.9 km s^{-1} for each line profile (cf. Fig. 6 in Paper I). Top panels show the window function and a centred zoom-in thereof. Note the reverse significance of the f_1, f_2, f_3 frequencies as compared to the photometry. f_1 is not visible for O II 4596 and is ambiguous in Si III 4553. The panels below show successive prewhitening of f_3 and f_2 respectively.

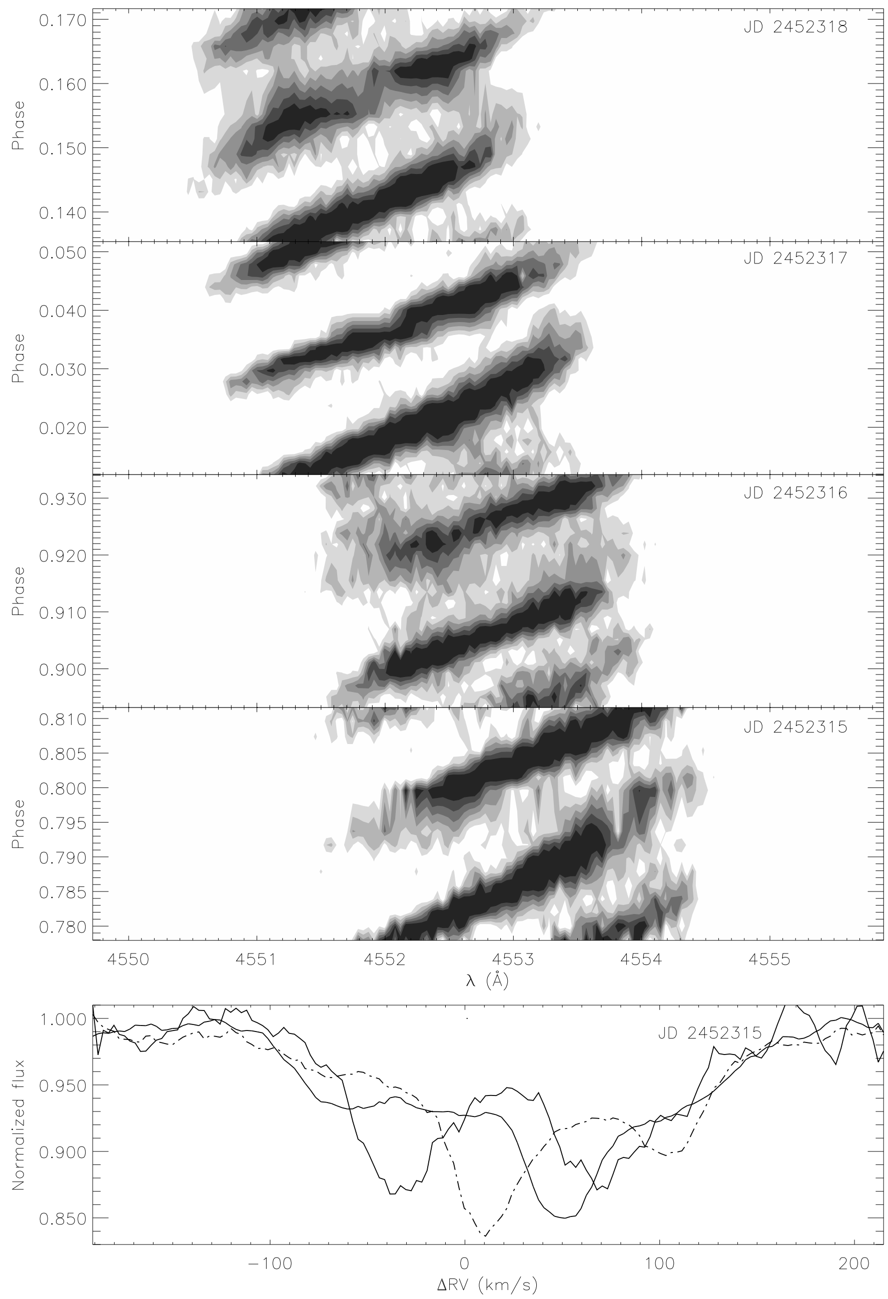

Figure 11: Line-shift and line-profile variations in Si III $\lambda\,4553$ relative to an average profile. The four upper panels are, from bottom to top, successive nights in 2002. Note the large and rapid pulsational LPVs in individual nights, as compared to the RV variations with orbital phase along the ordinate axis. The bottom panel shows the radial-velocity shifts in $\mathrm{km\,s^{-1}}$ from the laboratory wavelength for three smoothed spectra representative for the LPV variations.

4.3 Comments on the orbit from matched-spectrum RV differences

The FEROS and ECHELEC spectra were used to determine the orbital parameters summarised in Sect. 1. The ECHELEC spectra have lower quality and shorter wavelength range than the FEROS spectra, but as they cover some of the same orbital phases they are also valuable for testing orbit stability on the 13 yrs baseline.

The LPVs introduce bias in RVs (radial velocities) derived, for example, from straightforward cross correlation of spectra, and the velocity fields may shift such RVs up to 15 $\mathrm{km\,s^{-1}}$. In order to reduce the possible bias from the LPVs on the sought orbital parameters, Paper I introduced an alternative approach based on RV differences between spectra having similar line profiles. The detailed description is given in that paper. Here only a brief summary of the procedure is given. The RV differences were determined for all possible pairs of spectra by means of cross correlations and then, using the cross-correlation tables, the quality and mismatch of each two pair elements were evaluated with:

- Assuming that the line profiles at times t_i and t_j are not too different, the position of the maximum of the cross-correlation function $C(i, j; k)$ (see Paper I), for shifts of k pixels, estimates the difference in the RV of the star at t_i and t_j.
- $I_{\mathrm{SN}} = [\max \mathrm{C}(i, i; k) \times \max \mathrm{C}(j, j; k)]^{1/2}$, indicator of S/N of each pair, where the maxima of the auto-correlations are determined with a 3rd degree polynomial fit to $\mathrm{C}(i, i; 2 \leq |k| \leq 15)$.
- $I_{\mathrm{MM}} = I_{\mathrm{SN}} - \max \mathrm{C}(i, j; k)$, the mismatch of line profiles at times t_i and t_j. It simply expresses the deviation from the case with identical profiles.

Based on these indicators, 80 FEROS pairs were chosen as good matches. the difference between the two spectra in the 80 selected FEROS–FEROS pairs, corrected for orbital shift, is displayed in the He I λ4471 line (averaged profile at the top of the panel). The local line-profile mismatch is below 5% of the line depth, and typically far lower. The right panel shows the same for the same pairs of spectra, but with the elements disordered, resulting in profound mismatch above 30%. The left panel of Fig. 12 shows how well the selected pairs match;

Due to a larger smearing of the LPVs in the ECHELEC spectra, having 4 times longer exposure times, we averaged up to three consecutive FEROS spectra as *match templates* reproducing the line profiles of 23 ECHELEC spectra. For these cases the similarity was judged subjectively, but for the noisier

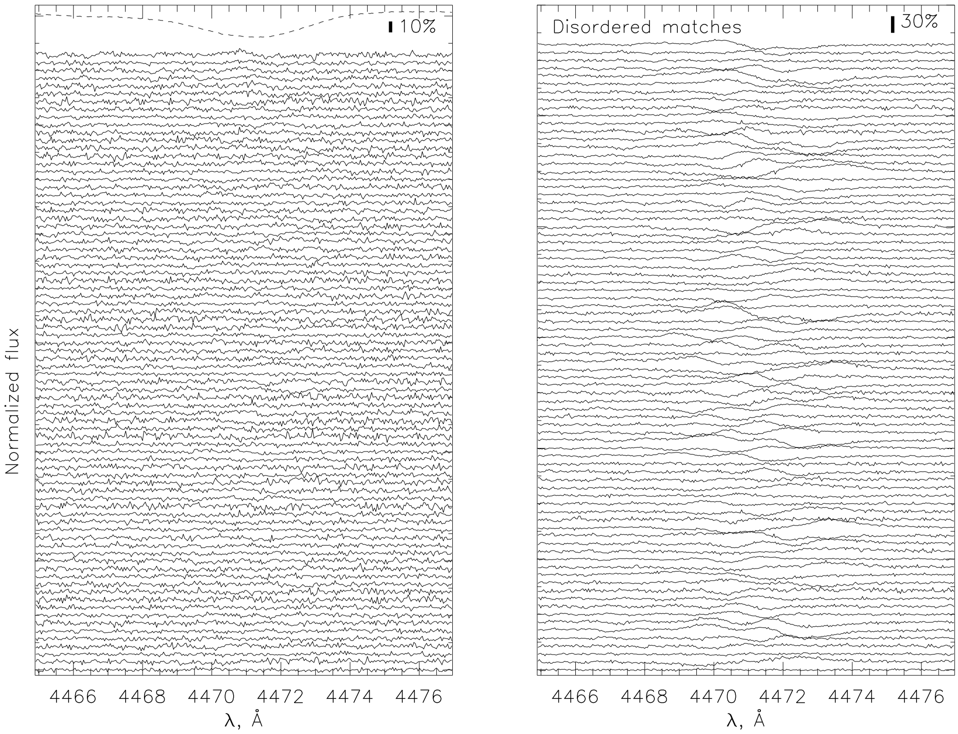

Figure 12: Quality of matching of FEROS spectra. Left: Residuals between matched FEROS spectra; the differences between pair elements of all 80 selected pairs of FEROS spectra. Wavelength region centred on the He I $\lambda\,4471$ line for spectra where orbital shift has been removed. Right: same as left panel, but for the differences between disordered pairs of same FEROS spectra. The residuals from the LPVs are clearly seen.

ECHELEC spectra, the similarity is evidently less stringent. Including these ECHELEC spectra, we had selected a total of 103 RV differences for pairs over 107 different orbital phases. These RV differences are listed in electronic form in Appendix A.4.

With least-square fitting to an eccentric Keplerian orbit these RV differences allow to optimise four parameters: the radial-velocity semi-amplitude $K_{\rm A}$; eccentricity e; time of periastron $t_{\rm peri}$ and longitude of periastron ω, the angular distance of periastron measured from the ascending node in the direction of orbital motion, by numerical iteration. Because photometry constrains ω stronger, we optimised e and ω iteratively in fitting the light-curve (ω) and the RV differences (e). The results are given in Table 6 and indicate a significant eccentricity. The rms of this solution is $4.0\,{\rm km\,s^{-1}}$ for pairs, corresponding to $2.8\,{\rm km\,s^{-1}}$ per pair element assuming random scatter. The corresponding model orbit is inserted in Fig. 13 (full line) and in the lower part of the top

Table 6: Orbital elements for HD 92024, P=8$^{\rm d}$.32457, derived from 107 RV differences (dRVs) fitted with a Keplerian orbit. The rms of the residuals to the solution, scaled to individual spectra, is $\sigma = 2.8$ km s^{-1}.

	dRVs
$t_{\rm peri}$ (HJD)	2 445 390.92±0.11
e	0.028 ± 0.005
ω	$64° \pm 5°$
$K_{\rm A}$	45.6 ± 0.5 km s^{-1}
$a_{\rm A} \sin i$	$5.23 \pm 0.06 \times 10^6$ km
$f(M)$	$0.0819 \pm 0.0045\,{\rm M}_\odot$

Table 7: Like Table 6 but for RVs, from cross correlation with the 103-spectrum template, fitted with SBOP. The fit was made with double weights on FEROS data. The scatter (σ) in Col. 2 of nightly averages was rescaled to single velocity measurements.

	RVs (SBOP, all data)	RVs (nightly avg.)
$t_{\rm peri}$ (HJD)	2 445 406.06±0.77	2 445 405.92±0.69
e	0.030 ± 0.014	0.026 ± 0.011
ω	$2° \pm 33°$	$357° \pm 30°$
$K_{\rm A}$	47.8 ± 0.8 km s^{-1}	47.8 ± 0.6 km s^{-1}
$a_{\rm A} \sin i$	$5.47 \pm 0.10 \times 10^6$ km	$5.47 \pm 0.07 \times 10^6$ km
$f(M)$	$0.0939 \pm 0.0050{\rm M}_\odot$	$0.0941 \pm 0.0038{\rm M}_\odot$
σ	5.1 km s^{-1}	3.9 km s^{-1}
# obs	125	14

panel, all phases for the used spectra are marked (solid squares).

How does this result compare with orbital parameters found from RVs obtained by straightforward cross correlation with a template spectrum? With the 103-spectrum composite as template spectrum, all FEROS and ECHELEC spectra were cross-correlated using the region λλ4584–4690 and the resulting RVs are shown in Fig. 13 (diamonds and solid dots) and given in Appendix A.5. The spectroscopic binary code SBOP (Etzel 1985) was applied to determine a spectroscopic solution for the RVs for fixed primary period. SBOP uses the methods of Lehmann-Filhés (1894). The solution (Table 7, Col. 2) is shown as a dashed line in Fig. 13 and differs from the previous solution by a larger semi-amplitude and also a different eccentricity. The eccentricity is again small but significant – in fact solving for a free period still indicates same value. The higher semi-amplitude is a result of the higher sensitivity to the pulsations; the large residuals (lower panel in Fig. 13) around velocity maxima of which one is

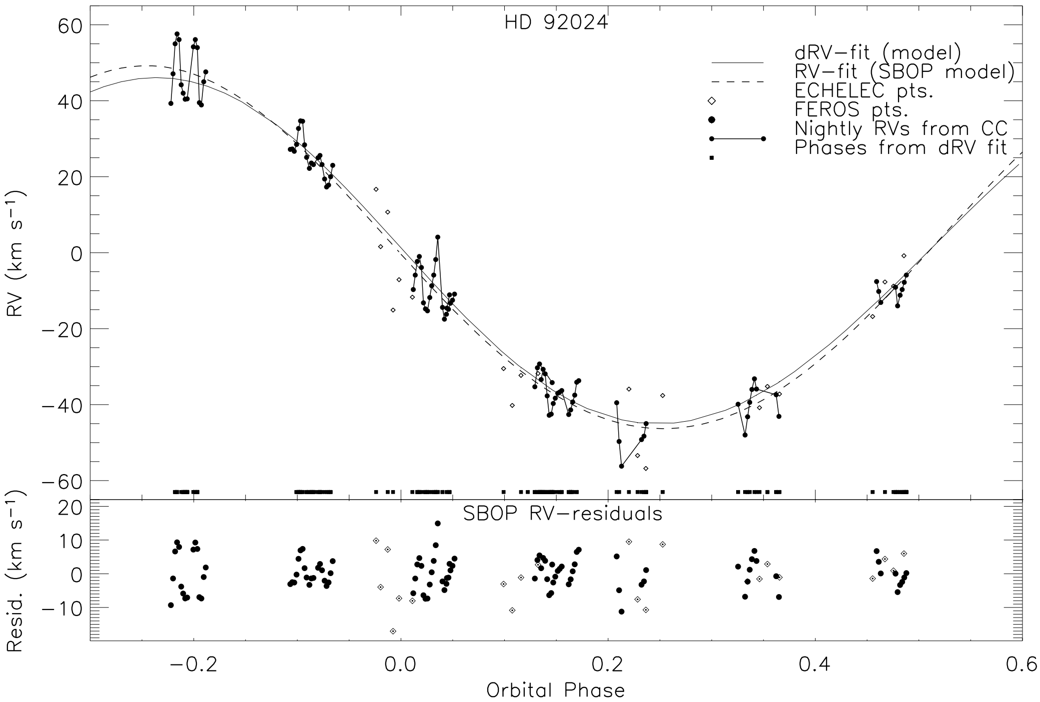

Figure 13: Top panel: The model orbit from RV differences (full line) and from RVs found from cross correlation with a template (dashed line). The systemic velocity is zero because all measurements are differential. FEROS RVs from the same night are connected by lines, making the LPVs appear clearly. Note the different velocity amplitudes of the two models. The lower panel gives the residuals for the SBOP model to the RVs from cross correlation with the 103-spectrum template.

not covered on both sides, leaves the fitting more freedom. A fit to the nightly RV averages was also made (Table 7, Col. 3) and found to support the previous SBOP solution, but with less scatter. Still, when considering the scatter in all procedures, the RV-difference orbital parameters seem the most reliable.

4.4 Comparison with spectra of σ Sco

It is well known that the line width in spectra of pulsating stars may include pulsational line broadening. The LPVs hamper direct comparison of spectral lines to synthetic model profiles that do not include velocity fields. Strength- and profile variations of lines, as caused by stellar pulsations, may be out of phase. This complicates an atmospheric parameter analysis.

The temperature of the primary $T_{\rm eff} = 25\,500 \pm 500\,$K (Paper I) suggests that HD 92024 is quite similar to the β Cephei component of the system σ Sco

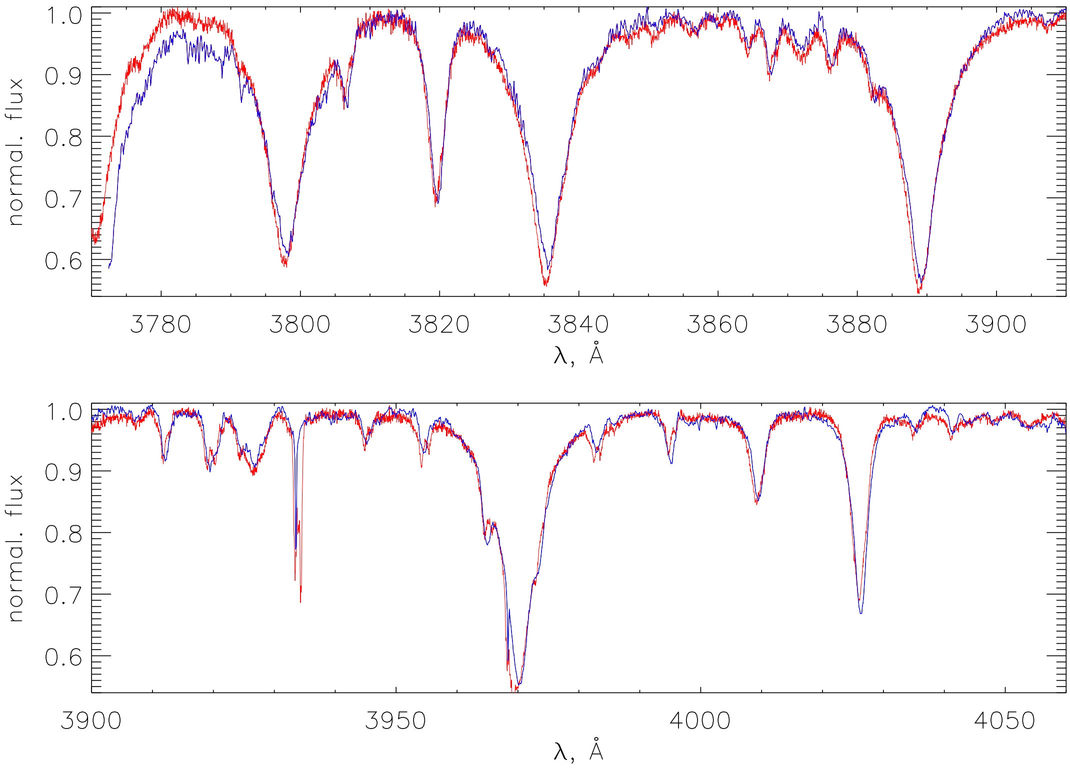

Figure 14: Comparison between a single ECHELEC spectrum of σ Sco (blue line) and a narrow-line spectrum composite of HD 92024 (red line). Notice the deeper interstellar Ca line for HD 92024, despite the orbital smearing. At the bluest wavelengths, the σ Sco spectrum was obviously normalised differently due to lack of continuum at the lowest wavelengths.

(=HD 147165, B1 III), which has effective temperature $T_{\rm eff} = 26\,150 \pm 1\,070$ K, $\log g = 3.85 \pm 0.17$ dex and near-solar He-N-O abundances (vander Linden & Butler 1988). The β Cephei component in σ Sco is the brightest component in a hierarchical triple system in a 33-day orbit with a $0\overset{\rm m}{.}4$ fainter star, and a $3\overset{\rm m}{.}4$ fainter companion in a 112 year, or longer, orbit. The latter star was detected by occultation (Nather et al. 1974). A fourth star at $20''$ separation is only an optical component. The spectrum is SB-2, but with very weak absorption from the faint secondary (Mathias et al. 1991).

We had two ECHELEC spectra of σ Sco (JD 2 448 399.8 and 2 448 720.8, 300s), obtained at air mass 1.10–1.12. Within the available wavelength range $\lambda\lambda$ 3790–4070 they were compared to those of HD 92024. The line shapes in one of the ECHELEC spectra matched those in our narrow-line spectrum composite of HD 92024, and the spectra could be compared directly (Fig. 14). Apart from the sharp interstellar Ca II-line, stronger for the more distant HD 92024, both spectra are remarkably similar. Within the limitations of the quality of the two spectra, we find no temperature difference. Thence, the similarity of the two spectra gives empirical support for the above temperature estimate from static atmosphere models.

5 Summary

We have provided carefully reduced spectra used for the analysis of HD 92024 in the work by Freyhammer et al. (2004), and given details on parts of the data reduction and data analysis. In addition a high-S/N spectrum was provided in Appendix B with line identification for the full wavelength range. The pronounced pulsational line variability combined with the long wavelength range provides a useful database for a preparatory asteroseismological analysis, such as intended for publication in Paper II.

Acknowledgements

This research was carried out in the framework of the 'IAP P5/36' project of the Belgian Federal Science Policy, and was supported by the Belgian Fund for Scientific Research (FWO) and the Flemish Ministry for Foreign Policy, European Affairs, Science and Technology, under contract BIL 01/2. In the framework of the project 'Structure and evolution of stars – new insight from eclipsing binaries and pulsating stars', support from the Danish National Science Research Council is acknowledged. We have made use of the Simbad database, operated by the CDS, Strasbourg, France, the `ESO-MIDAS` and `NOAO-IRAF` software, the SBOP and the Wilson-Devinney codes.

References

Balona, L.A. 1975, MmRAS, 78, 51

Coluzzi, R. 1993, A revised version of the ILLSS Catalogue, Bull. Inf. CDS 43, 7

Daflon, S., Cunha, K., Becker, S.R. & Smith, V.V. 2001, ApJ, 552, 309

Engelbrecht, C.A. 1986, MNRAS, 223, 189

Engelbrecht, C.A. & Balona, L.A. 1986, MNRAS, 219, 449

Etzel P.B. 1985, SBOP – Spectroscopic Binary Orbit Program, Program's Manual

Freyhammer, L.M., Arentoft, T. & Sterken, C. 2001, A&A 368, 580

Freyhammer, L.M., Hensberge, H., Sterken, C., et al. 2004, Paper I, A&A, accepted

Hensberge, H. 2001, Report, http://www.astro.oma.be/common/research/dep3/publications/HH-FEROS-PipeEval.ps.gz

Hensberge, H. 2004, in *Spectroscopically and Spatially Resolving the Components of Close Binary Stars* (eds. R.W. Hilditch, H. Hensberge & K. Pavlovski), ASP Conf. Ser. 318, 41

Jenniskens, P. & Désert, X. 1994, A&AS, 106, 39

Jerzykiewicz, M., Jarzebowski, T., Musielok, B. & Le Contel, J.M. 1978, IBVS, 1508, 1

Jerzykiewicz, M. & Sterken, C. 1992, MNRAS, 257, 303 (JS92)

Kaltcheva, N.T 2003, A&A, 410, 523

Kwee, K.K. & van Woerden, H. 1956, Bull.Astron.Neth., 12, 323

Lafler, J. & Kinman, T.D. 1965, ApJS, 11, 216

Lehmann-Filhés, R., 1894, Astron. Nach. 136, 17

Martin, W.C., Fuhr, J.R., Kelleher, D.E., Musgrove, A., et al. 1999. Atomic Spectra Database (vers. 2.0), (http://physics.nist.gov/asd) Nat. Institute of Standards and Technology, Gaithersburg, MD

Mathias, P., Gillet, D. & Crowe, R. 1991, A&A 252, 245

Meinel, A.B., Aveni, A.F. & Stockton, M.W. 1969, Catalog of spectral emission lines of astrophysical objects (2nd edition), Optical Sciences Center and Steward Observatory, Tucson, Arizona

Moore, C.E. 1959, NBS Technical Note 36

Nather, R.E., Churms, J. & Wild, P.A.T. 1974, PASP 86, 509, 116

Schrijvers, C,. Telting, J.H. & Aerts, C. 2004, A&A, 416, 1069

Shobbrook, R.R. 1983, MNRAS, 205, 1215

Skoda, P. & Hensberge, H. 2003, in ADASS XII (eds. H.E. Payne, R.I. Jedrzejewski & R.N. Hook), ASP Conf. Ser. 295, 415

Sperl, M. 1998, Communications in Asteroseismology, Univ. of Vienna, 111, 1

Sterken, C. 1983, The ESO Messenger 33, 10

vander Linden, D. & Butler, K. 1988, A&A, 189, 137

Verschueren, W., Brown, A.G.A., Hensberge, H., David, M., et al. 1997, PASP, 109, 868

Appendix

A Final, reduced spectra

As electronic versions in FITS-format, the 103 FEROS and 23 ECHELEC spectra are given in reduced form, as described in Sect. 2.1. A conservative cosmic-ray rejection procedure was performed for the FEROS spectra. The ECHELEC spectra were corrected for severe blemishes and were therefore applied an extra correction, as described in Sect. 2.1. Shifts applied to these spectra include barycentric wavelength correction, and telluric line correction tracing small offsets between the science and ThAr and Ne lamps spectra (See Sect. 2.1 and Appendix A.1). The original 2D FEROS spectra and calibration sets are available on request.

A.1 FITS-header content of FEROS spectra

The FEROS fits headers have the following typical content:

```
SIMPLE  =                    T / Standard FITS format: NOST 100-2.0
BITPIX  =                  -32 / No. of bits per pixel
NAXIS   =                    1 / No. of axes in image
NAXIS1  =               103013 / No. of pixels
EXTEND  =                    T / FITS extension may be present
BLOCKED =                    T / FITS file may be blocked
CRPIX1  =                   1. / Reference pixel
CRVAL1  =           8.18011817 / Coordinate at reference pixel
CDELT1  =             9.09E-06 / Coord. incr. per pixel (original value)
CTYPE1  = 'UNITLESS        '   / Units of coordinate
BUNIT   = 'Unitless        '   / Units of data values
DATAMAX =        1.39825439453 / Maximum data value
DATAMIN =      -0.802870631218 / Minimum data value
ORIGIN  = 'ESO-MIDAS'          / Written by MIDAS
DATE    = '2004-07-13T12:03:15' /  [UTC] Date of writing
FILENAME= 'ln9999.fits'        / Original file base-name
MIDASFTP= 'IMAGE   '           / MIDAS File Type
OBJECT  = 'HD 92024'           / MIDAS desc.: IDENT(1)
RA      =            159.09911 / MIDAS desc.: O_POS(1)
DEC     =            -58.22644 / MIDAS desc.: O_POS(2)
DATE-OBS= '2001-02-19'         / MIDAS desc.: O_TIME(1)
TM-START=               30171. / MIDAS desc.: O_TIME(5)
EXPTIME =                1200. / MIDAS desc.: O_TIME(7)
TELESCOP= 'ESO-1.52'           / MIDAS desc.: TELESCOP(1)
INSTRUME= 'FEROS   '           / MIDAS desc.: INSTRUME(1)
```

```
OBSERVAT= 'ESO-LASILLA'
DETNAME = 'EEV 2k x 4k'
TM_START=                30171 / 08/22/51           UT start time
TM_END  =                31525 / 08/45/25           UT end time
GAINM   = 'LOW     '           / High or Low
AMPLM   = 'B       '           / A / B or AB
CCDTEMP =               -140.1
LN2TEMP =               -137.4
MPP     =                    0
CHIPID  = 'EEV 2Kx4K, FEROS'
XOVERSC =                    0
YOVERSC =                    0
P_DEWAR =             3.3E-05
SHSTAT  = 'OPEN    '
INSTR   = 'FEROS   '           / Slit  Configuration
F_MODE  = 'OS      '           / Fiber Configuration
EXPTYPE = 'SCIENCE '           / Exposure Type
CFM_POS = 'OUT     '           / Calibration Mirror
RSM_POS = 'S3      '           / Calib. Source Mirror
FFU     = 'OFF     '           / Flatfield lamp
WCU1    = 'OFF     '           / Thorium-Argon lamp
WCU2    = 'OFF     '           / Helium-Argon lamp
NDFW    =                1.004 / Neutral Density Filter
CIDENT  = '         HD92024'   / Object name from catalogue
RA-OBJ  = '        1036 8.30'  / Object Right Ascension
ST      =             13.62865 / Sidereal time at start
HA      =             45.33065 / Telescope Hour Angle at start
ZDIST   =             42.35339 / Telescope Zenith distance at start
TSPEC   =                18.06 / Temperature of Spectrograph
TROOM   =                16.95 / Temperature of Room
RHROOM  =                50.77 / rel.Humidity of Room
MTIME   = 'Feb 19 2001, 05:18' / DATE/LT  of T/RH Measurement
ORB-PHAS=                14.79
TLC     =                -0.02
SN-RATIO=                61.79
MID-HJD =        2451959.85814
WCSDIM  =                    1
CD1_1   =             9.09E-06
LTM1_1  =                   1.
HISTORY  ESO-DESCRIPTORS START   ................
HISTORY  'BARY_CORR','R*4',1,1,'5E14.7'
HISTORY   1.1571558E+01
HISTORY
HISTORY  'REBINFRA','C*1',1,80,'70A1'
```

```
HISTORY  rebin/feros corfsm4803ext ThAr4803final rs4803ext
HISTORY
HISTORY  'REBINPAR','C*1',1,80,'70A1'
HISTORY  0 9.090000276046339E-06,1.155155754089355E+01 S
HISTORY
HISTORY  'LHCUTS','R*4',1,4,'5E14.7'
HISTORY  -1.0000000E-02 1.0500000E+00-8.0287063E-01 1.3982544E+00
HISTORY
HISTORY  ESO-DESCRIPTORS END     ................
```

A few of these keywords are documented below.

Keyword(s)	Comment(s)
CDELT1	Pixel, or element, size in ln λ (Å)
CTYPE1	Coordinates are wavelength in ln λ (Å)
BUNIT	Flux is given as normalised flux
FILENAME	File name with 4-digit number preserved from original ESO ID
TM-START	UT in number of seconds at start of exposure
EXPTIME	Exposure time in seconds
MID-HJD	Mid-exposure Heliocentric Julian date (days)
TLC	Telluric Line Correction ($\mathrm{km\,s^{-1}}$) (Sect. 2.1)
ORB-PHAS	Orbital Phase
SN-RATIO	rough estimate of S/N ratio around 4500 Å
HISTORY 'BARY_CORR'	(for `MIDAS`) Barycentric correction ($\mathrm{km\,s^{-1}}$) as added to the spectra
HISTORY 'LHCUTS'	(for `MIDAS`) default intensity cuts for plotting the data (first two elements)

A.2 FEROS spectra

Note! These 1-D spectra have been treated with a cosmic ray rejection routine that in exceptional cases may damage the sharpest and strongest telluric line profiles.

A.3 ECHELEC spectra

A.4 Radial-velocity differences in table format

`RVDIFFS.DAT` Note that for the pairs including an ECHELEC element, the corresponding FEROS element is a composite of 1–4 spectra as stated in Table 8. '9999' in Col. 2 of `RVDIFFS.DAT` indicates these cases, and the corresponding times and phases are mean values over the composite elements.

Table 8: Matching FEROS templates (Col. 4) for the ECHELEC spectra (Col. 1) with corresponding orbital phases, see also file RVDIFFS.DAT.

SPECA	PHASE_A	PHASE_B	SPECB FEROS COMPOSITE
116	0.976008	0.921901	5153,5154,5155
121	0.987228	0.803479	5077,5078,5080,5081
122	0.992396	0.914530	5151,5152
131	0.011078	0.921901	5153,5154,5155
208	0.099092	0.150181	5304,5306
212	0.115911	0.027719	5227,5228,5229
213	0.122434	0.803464	5079
219	0.132346	0.029706	5229
312	0.220095	0.899130	5142,5143,5144
313	0.228451	0.905051	5145,5146,5147
314	0.236447	0.912572	5150,5151
322	0.252668	0.915546	5152
412	0.334435	0.913563	5150,5151,5152
414	0.346121	0.916351	5151,5152,5153
415	0.353776	0.923833	5155,5157
415	0.353776	0.926330	5157
420	0.365410	0.915170	5150,5151,5152,5153
519	0.455351	0.018764	5223,5224
523	0.467228	0.016772	5222,5223
525	0.475480	0.017768	5222,5223,5224
601	0.485561	0.137294	5297,5298,5299

A.5 Radial velocities in table format

`RVS.DAT`

A.6 103-spectrum composite, with DIBs

`TEMPL103.FIT` (fits-file)

B Line atlas of HD 92024

The following figures show the line region 3700–8600 Å of HD 92024 for a 103-spectrum composite, using all FEROS spectra. This spectrum (Appendix A.5) differs from our 103-spectrum template by not having DIBs removed prior to combination. This composite reaches $S/N \approx 1\,000$. Orbital shifts for all 103 FEROS spectra of HD 92024, were removed with the model in Paper I before combining all spectra. Non-stellar features such as telluric and interstellar lines and DIBs are subjected to smearing from the ± 50 km s^{-1} shifts (± 0.7Å). The LPVs are averaged and lines appear 'box'-shaped.

A shift of $+16$ km s^{-1} was applied to remove the systemic velocity, such that the lines essentially coincide with laboratory wavelengths (in air). A smoothing of 2 pixels was applied over the composite spectrum. A few emission-like blemishes are apparent in the spectrum (see Table 1). We remark here that the following line region seems optimal for cross correlation as based on information content and quality: 4207–4733 Å.

In the figures wavelength is given as λ in Å and $\ln \lambda$ in the bottom and top of each panel, respectively. Whenever deep lines are present, the same spectrum is overplotted in blue colour, scaled to 30% of the default normalised absorption scale, as indicated by the scale at the r.h. side of these graphs. DIBs are marked with horizontal dashed lines of length $\pm 2 \times$ FWHM (based on Jenniskens & Désert 1994). Stellar line identifications are made using the catalogues by Coluzzi (1993), Daflon et al. (2003), Martin et al. (1999) and Moore (1959). Emission lines identified in the sky spectra are labelled as sky emission lines. For $\lambda > 6860$ Å, regions densely populated by telluric lines are not shown as smearing by the orbital velocity shifts destroys the telluric spectra. The regions concerned are: $\lambda\lambda$ 6860–7055, 7170–7370, 7590-7700, 8100–8400. Several figures for $\lambda > 6000$ Å are presented with approximately twice the range in wavelength per Figure.

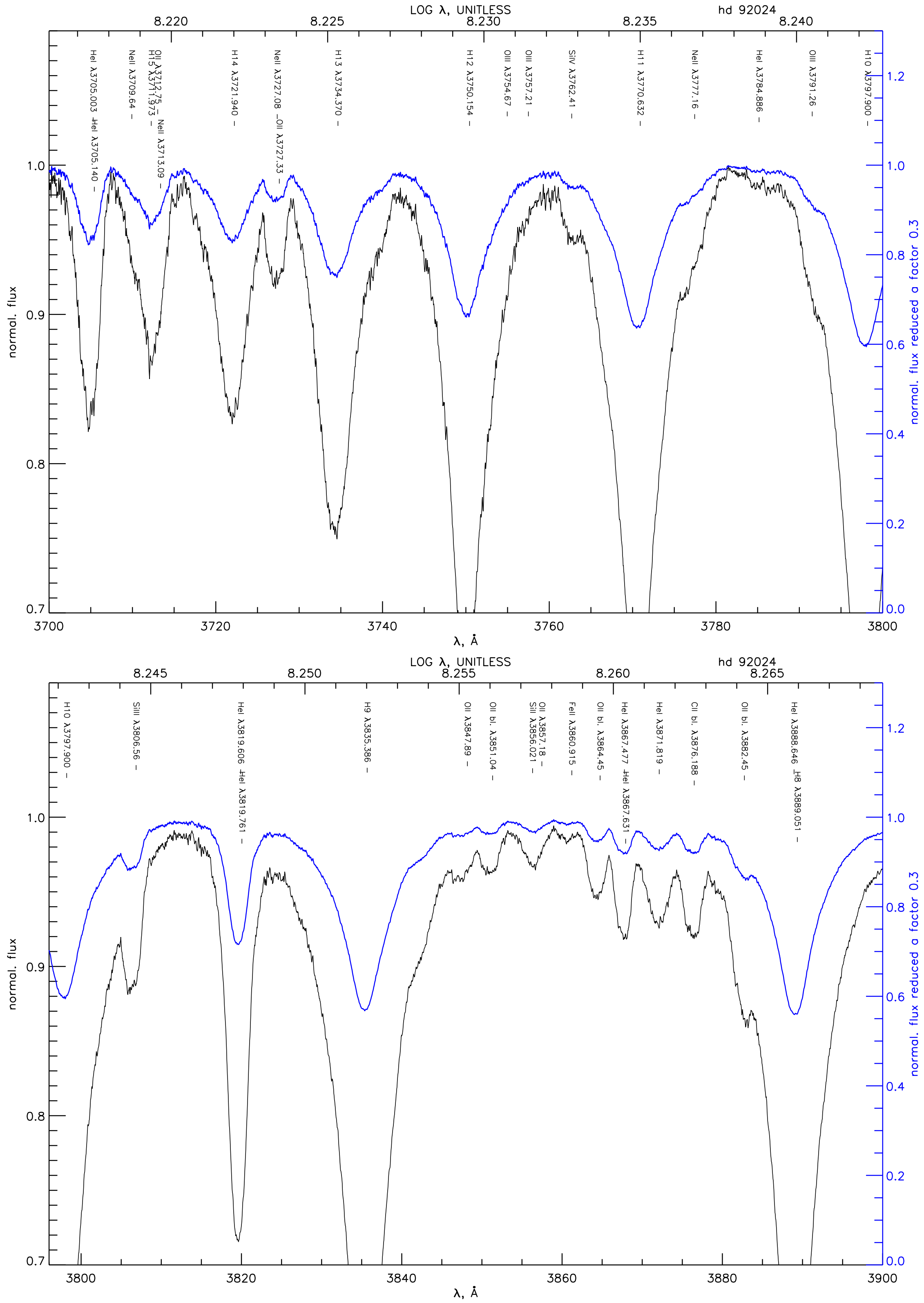
LOG λ, UNITLESS
hd 92024
normal. flux
normal. flux reduced a factor 0.3
λ, Å
HeI λ3705.003 HeI λ3705.140
NeII λ3709.64
OII λ3712.75
H15 λ3711.973
NeII λ3713.09
H14 λ3721.940
NeII λ3727.08 OII λ3727.33
H13 λ3734.370
H12 λ3750.154
OIII λ3754.67
OIII λ3757.21
SiIV λ3762.41
H11 λ3770.632
NeII λ3777.16
HeI λ3784.886
OIII λ3791.26
H10 λ3797.900
SiIII λ3806.56
HeI λ3819.606 HeI λ3819.761
H9 λ3835.386
OII λ3847.89
OII bl. λ3851.04
OII λ3857.18
SiII λ3856.021
FeII λ3860.915
OII bl. λ3864.45
HeI λ3867.477 HeI λ3867.631
HeI λ3871.819
CII bl. λ3876.188
OII bl. λ3882.45
HeI λ3888.646 H8 λ3889.051

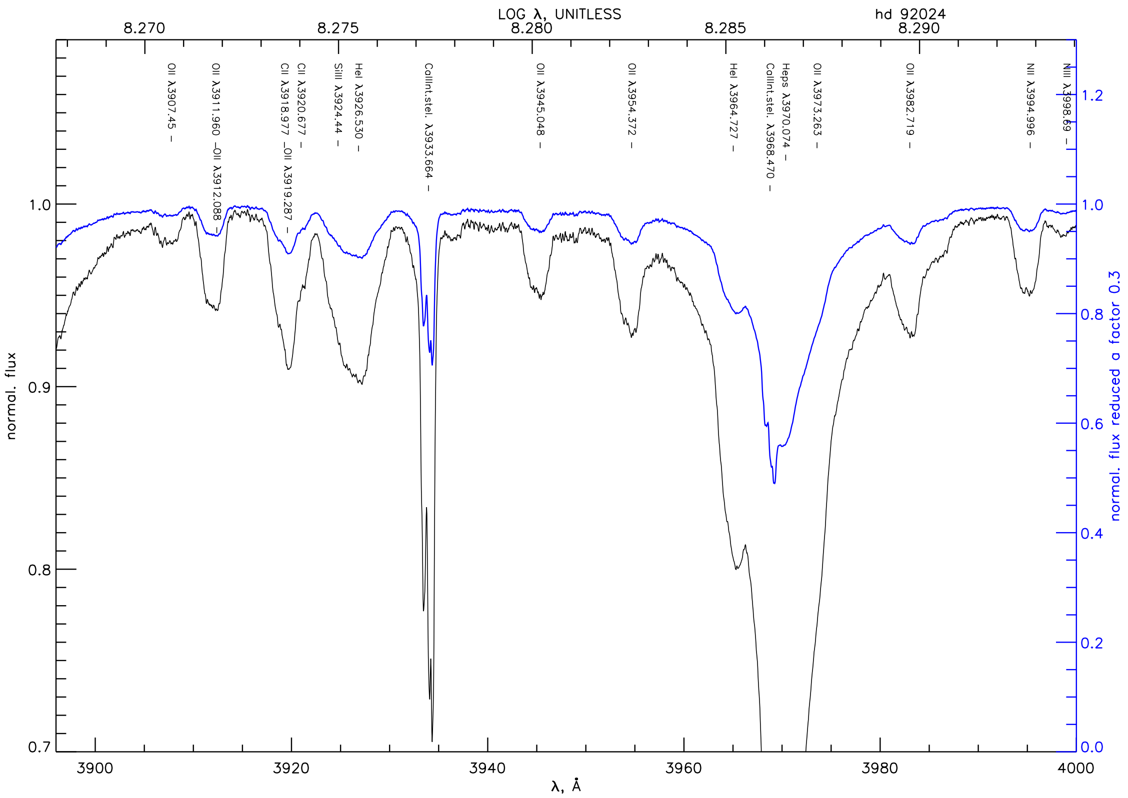
LOG λ, UNITLESS
hd 92024
8.270
8.275
8.280
8.285
8.290
OII λ3907.45
OII λ3911.960
OII λ3912.088
CII λ3918.977
OII λ3919.287
CII λ3920.677
SiIII λ3924.44
HeI λ3926.530
CaIIint.stel. λ3933.664
OII λ3945.048
OII λ3954.372
HeI λ3964.727
CaIIint.stel. λ3968.470
Heps λ3970.074
OII λ3973.263
OII λ3982.719
NII λ3994.996
NIII λ3998.69
normal. flux
normal. flux reduced a factor 0.3
λ, Å
3900
3920
3940
3960
3980
4000

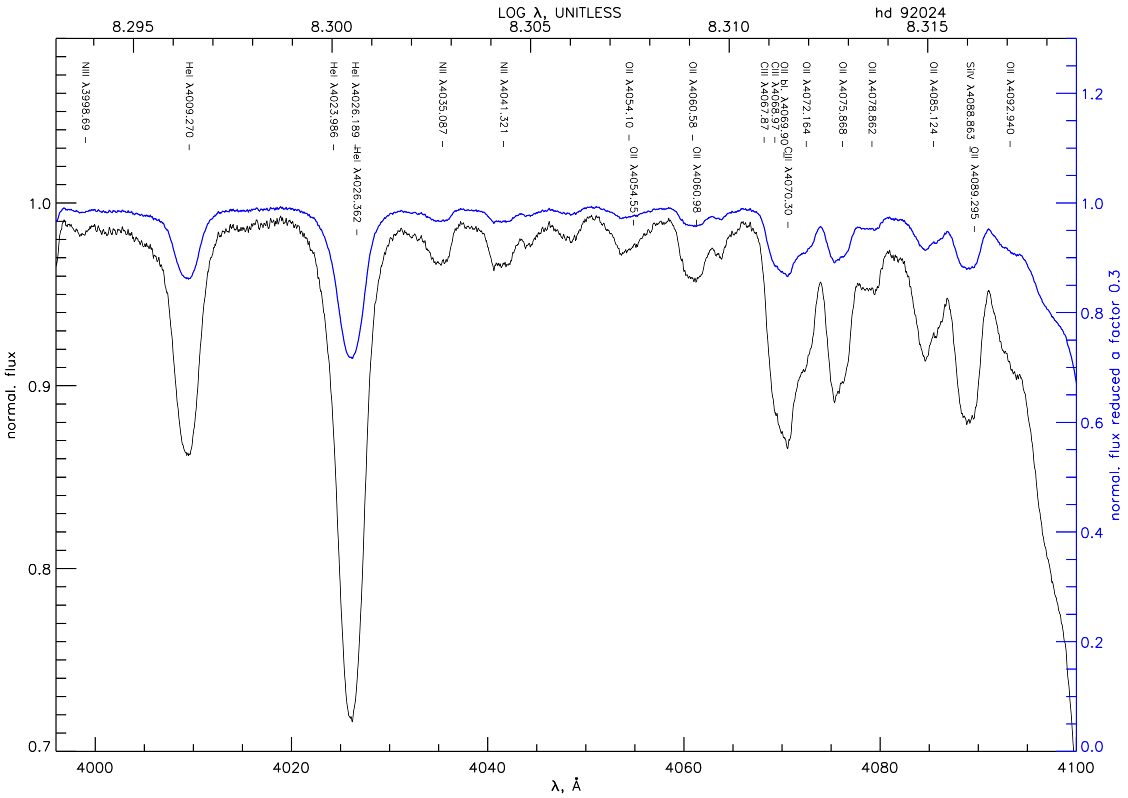
LOG λ, UNITLESS
hd 92024
8.295
8.300
8.305
8.310
8.315
NIII λ3998.69
HeI λ4009.270
HeI λ4023.986
HeI λ4026.189
HeI λ4026.362
NII λ4035.087
NII λ4041.321
OII λ4054.10
OII λ4054.55
OII λ4060.58
OII λ4060.98
CIII λ4067.87
CIII λ4068.97
OII bl. λ4069.90
OII λ4070.30
OII λ4072.164
OII λ4075.868
OII λ4078.862
OII λ4085.124
SiIV λ4088.863
OII λ4089.295
OII λ4092.940
normal. flux
normal. flux reduced a factor 0.3
λ, Å
4000
4020
4040
4060
4080
4100

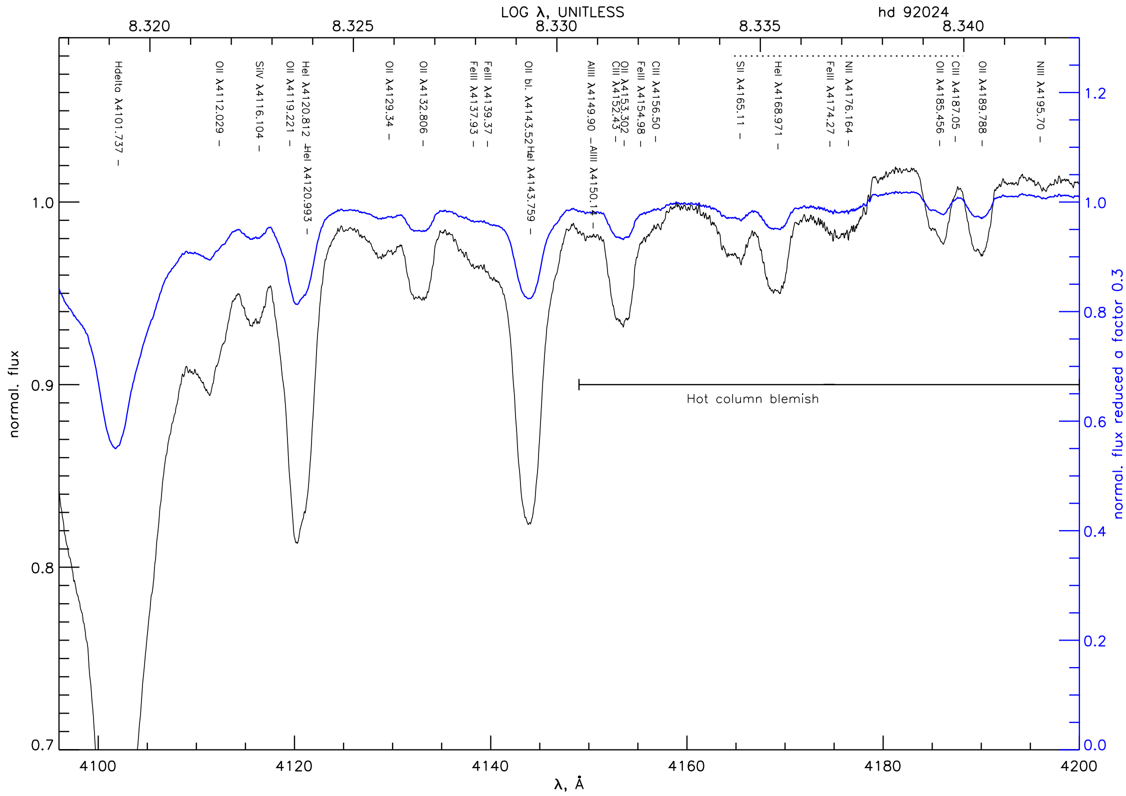
LOG λ, UNITLESS
hd 92024
8.320
8.325
8.330
8.335
8.340
Hdelta λ4101.737
OII λ4112.029
SiIV λ4116.104
OII λ4119.221
HeI λ4120.812
HeI λ4120.993
OII λ4129.34
OII λ4132.806
FeIII λ4137.93
FeIII λ4139.37
OII bl. λ4143.52
HeI λ4143.759
AlIII λ4149.90
AlIII λ4150.1
CII λ4152.43
OII λ4153.302
FeIII λ4154.98
CIII λ4156.50
SII λ4165.11
HeI λ4168.971
FeIII λ4174.27
NII λ4176.164
OII λ4185.456
CIII λ4187.05
OII λ4189.788
NIII λ4195.70
Hot column blemish
normal. flux
normal. flux reduced a factor 0.3
λ, Å

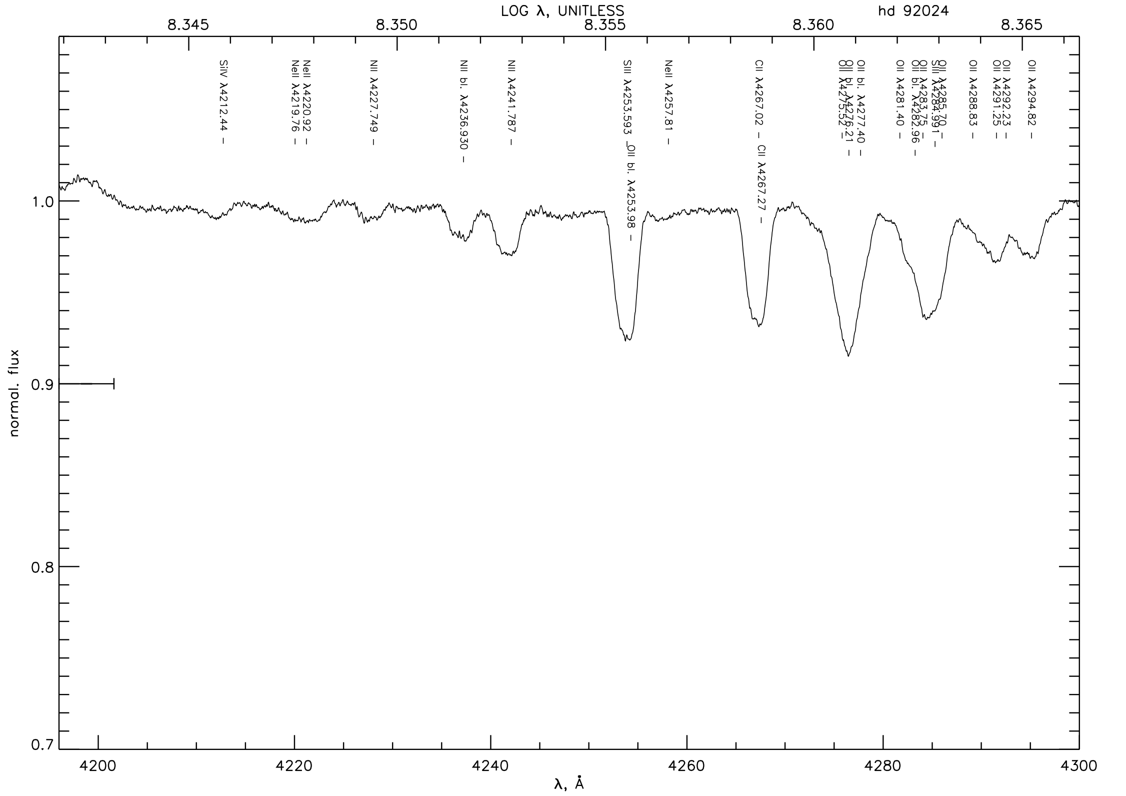
LOG λ, UNITLESS
hd 92024
8.345
8.350
8.355
8.360
8.365
SiIV λ4212.44
NeII λ4219.76
NeII λ4220.92
NII λ4227.749
NII bl. λ4236.930
NII λ4241.787
SIII λ4253.593
OII bl. λ4253.98
NeII λ4257.81
CII λ4267.02
CII λ4267.27
OII bl. λ4277.40
OII λ4281.40
OII bl. λ4282.96
OII λ4283.75
OII λ4288.83
OII λ4291.25
OII λ4292.23
OII λ4294.82
normal. flux
λ, Å

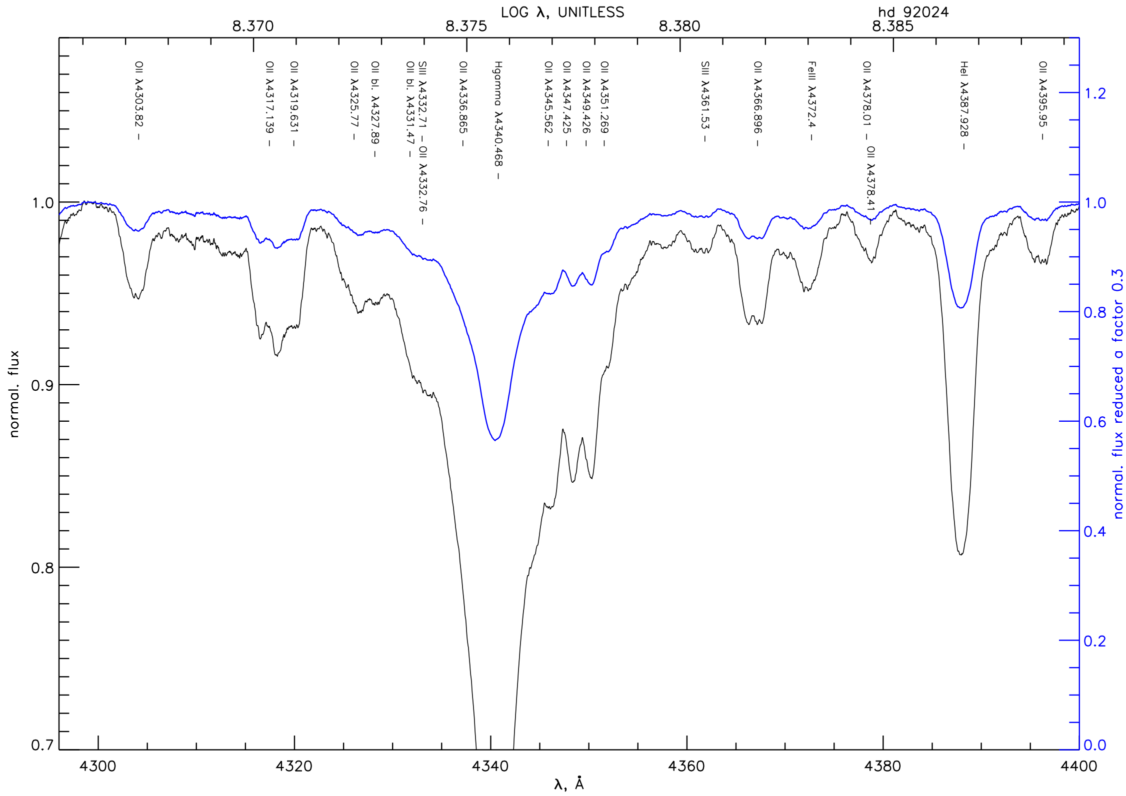
LOG λ, UNITLESS
hd 92024
8.370
8.375
8.380
8.385
OII λ4303.82
OII λ4317.139
OII λ4319.631
OII λ4325.77
OII bl. λ4327.89
OII bl. λ4331.47
SiIII λ4332.71 – OII λ4332.76
OII λ4336.865
Hgamma λ4340.468
OII λ4345.562
OII λ4347.425
OII λ4349.426
OII λ4351.269
SiIII λ4361.53
OII λ4366.896
FeIII λ4372.4
OII λ4378.01 – OII λ4378.41
HeI λ4387.928
OII λ4395.95
normal. flux
normal. flux reduced a factor 0.3
1.0
0.9
0.8
0.7
1.2
1.0
0.8
0.6
0.4
0.2
0.0
4300
4320
4340
4360
4380
4400
λ, Å

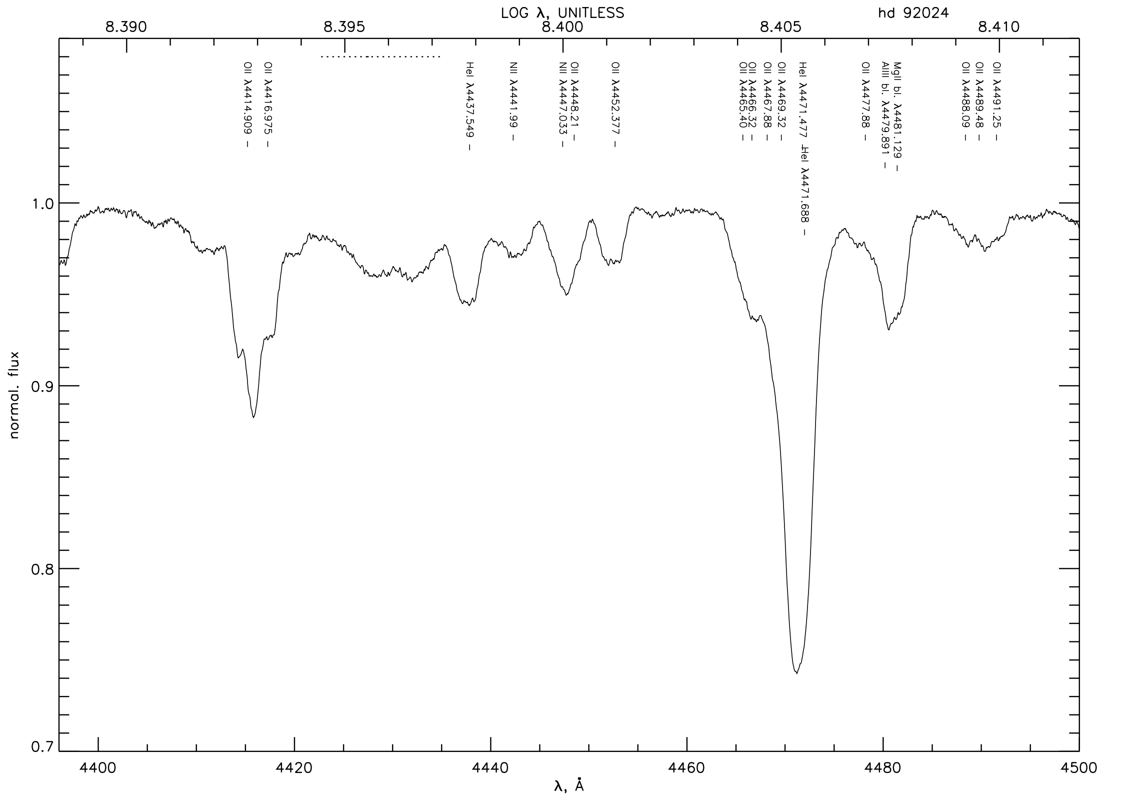
LOG λ, UNITLESS
hd 92024
8.390
8.395
8.400
8.405
8.410
OII λ4414.909
OII λ4416.975
HeI λ4437.549
NII λ4441.99
NII λ4447.033
OII λ4448.21
OII λ4452.377
OII λ4465.40
OII λ4466.32
OII λ4467.88
OII λ4469.32
HeI λ4471.477
HeI λ4471.688
OII λ4477.88
AlIII bl. λ4479.891
MgII bl. λ4481.129
OII λ4488.09
OII λ4489.48
OII λ4491.25
normal. flux
1.0
0.9
0.8
0.7
4400
4420
4440
4460
4480
4500
λ, Å

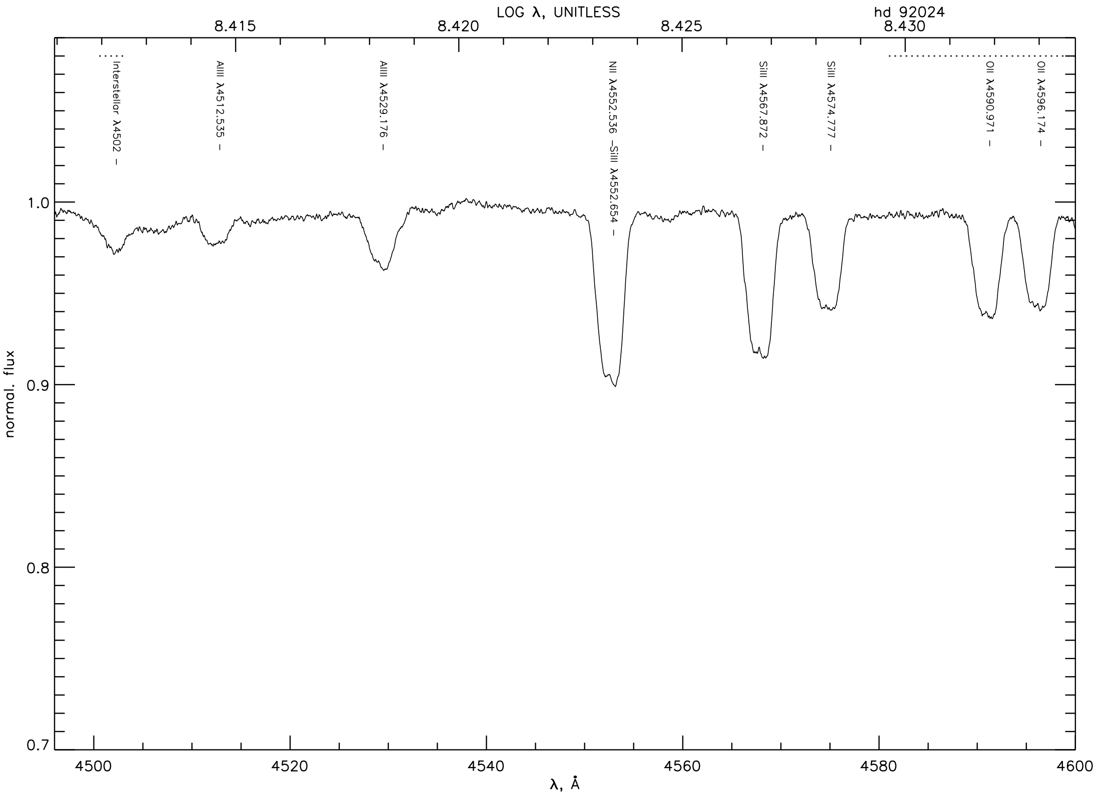
LOG λ, UNITLESS
hd 92024
8.415
8.420
8.425
8.430
Interstellar λ4502
AlIII λ4512.535
AlIII λ4529.176
NII λ4552.536 –SiIII λ4552.654
SiIII λ4567.872
SiIII λ4574.777
OII λ4590.971
OII λ4596.174
normal. flux
1.0
0.9
0.8
0.7
4500
4520
4540
4560
4580
4600
λ, Å

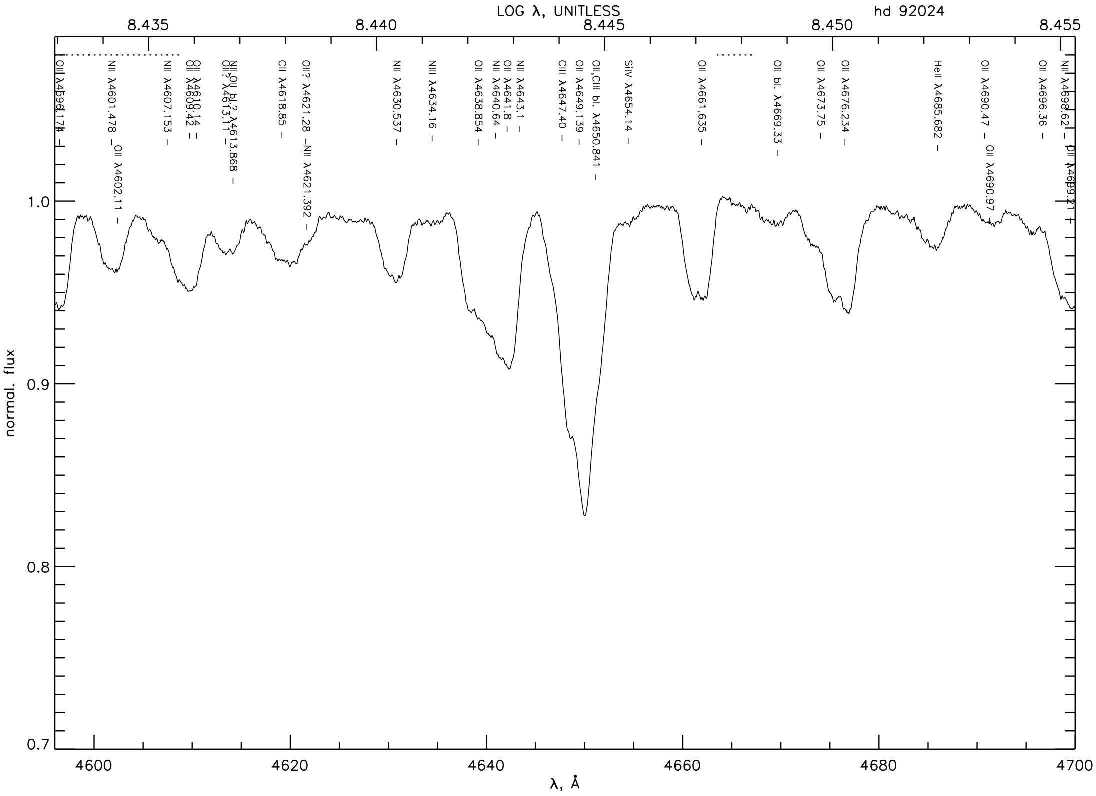
LOG λ, UNITLESS
hd 92024
8.435
8.440
8.445
8.450
8.455
NII λ4601.478 – OII λ4602.11
NII λ4607.153
CII λ4618.85
OII? λ4621.28 – NII λ4621.392
NII λ4630.537
NIII λ4634.16
OII λ4638.854
NII λ4640.64
OII λ4641.8
NII λ4643.1
CIII λ4647.40
OII λ4649.139
OII,CIII bl. λ4650.841
SiIV λ4654.14
OII λ4661.635
OII bl. λ4669.33
OII λ4673.75
OII λ4676.234
HeII λ4685.682
OII λ4690.47 – OII λ4690.97
OII λ4696.36
normal. flux
1.0
0.9
0.8
0.7
4600
4620
4640
4660
4680
4700
λ, Å

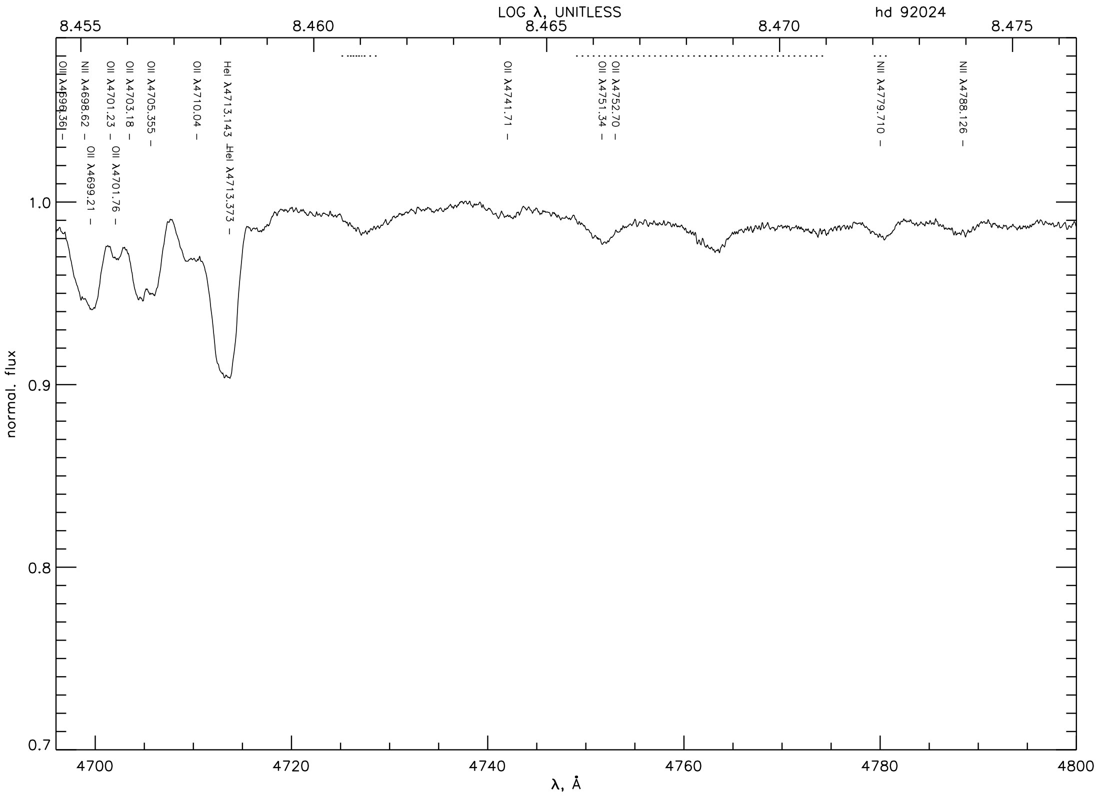
LOG λ, UNITLESS
hd 92024
8.455
8.460
8.465
8.470
8.475
NII λ4698.62
OII λ4699.21
OII λ4701.23
OII λ4701.76
OII λ4703.18
OII λ4705.355
OII λ4710.04
HeI λ4713.143
HeI λ4713.373
OII λ4741.71
OII λ4751.34
OII λ4752.70
NII λ4779.710
NII λ4788.126
normal. flux
1.0
0.9
0.8
0.7
4700
4720
4740
4760
4780
4800
λ, Å

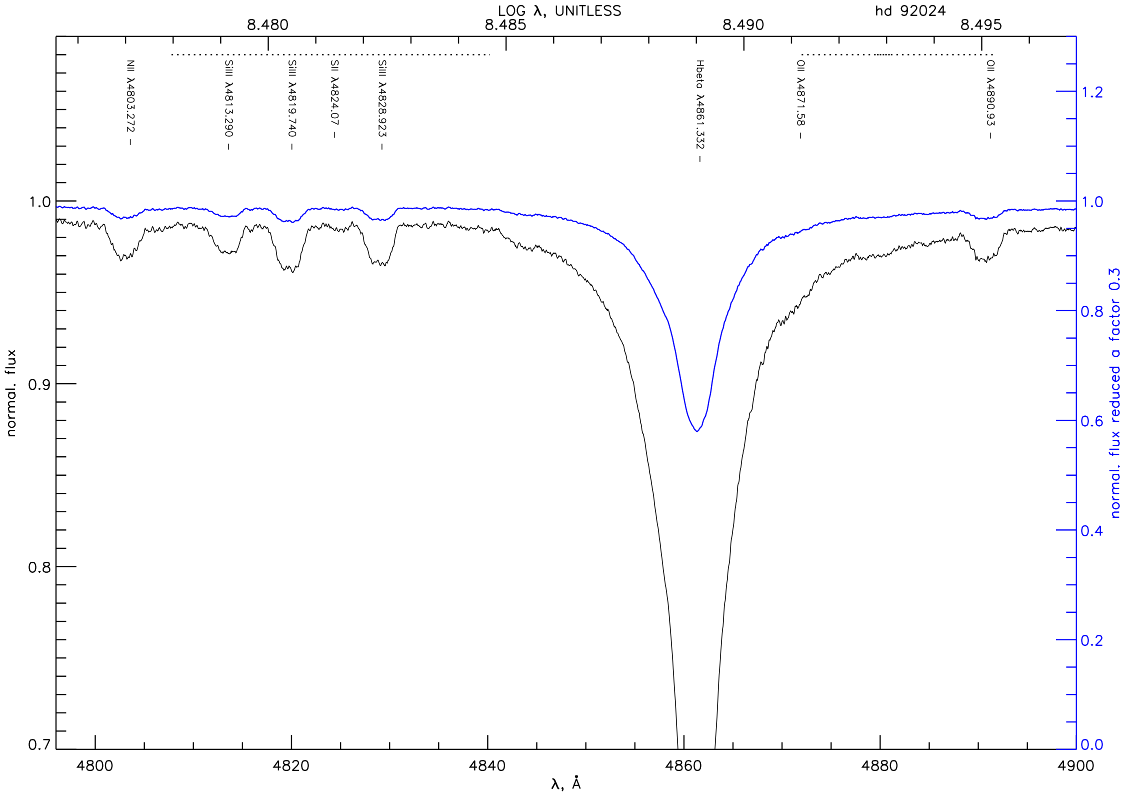
LOG λ, UNITLESS
hd 92024
8.480
8.485
8.490
8.495
NII λ4803.272
SiIII λ4813.290
SiIII λ4819.740
SII λ4824.07
SiIII λ4828.923
Hbeta λ4861.332
OII λ4871.58
OII λ4890.93
normal. flux
1.0
0.9
0.8
0.7
normal. flux reduced a factor 0.3
1.2
1.0
0.8
0.6
0.4
0.2
0.0
4800
4820
4840
4860
4880
4900
λ, Å

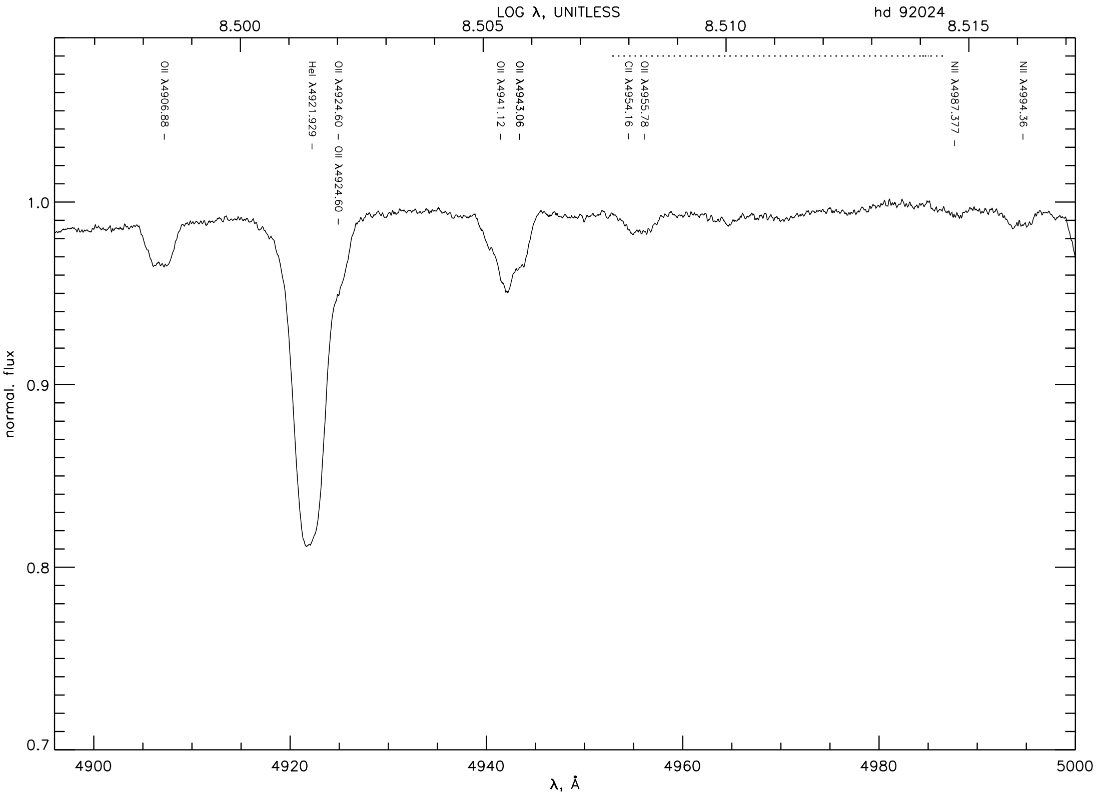
LOG λ, UNITLESS
hd 92024
8.500
8.505
8.510
8.515
OII λ4906.88
HeI λ4921.929
OII λ4924.60
OII λ4924.60
OII λ4941.12
OII λ4943.06
CII λ4954.16
OII λ4955.78
NII λ4987.377
NII λ4994.36
normal. flux
1.0
0.9
0.8
0.7
4900
4920
4940
4960
4980
5000
λ, Å

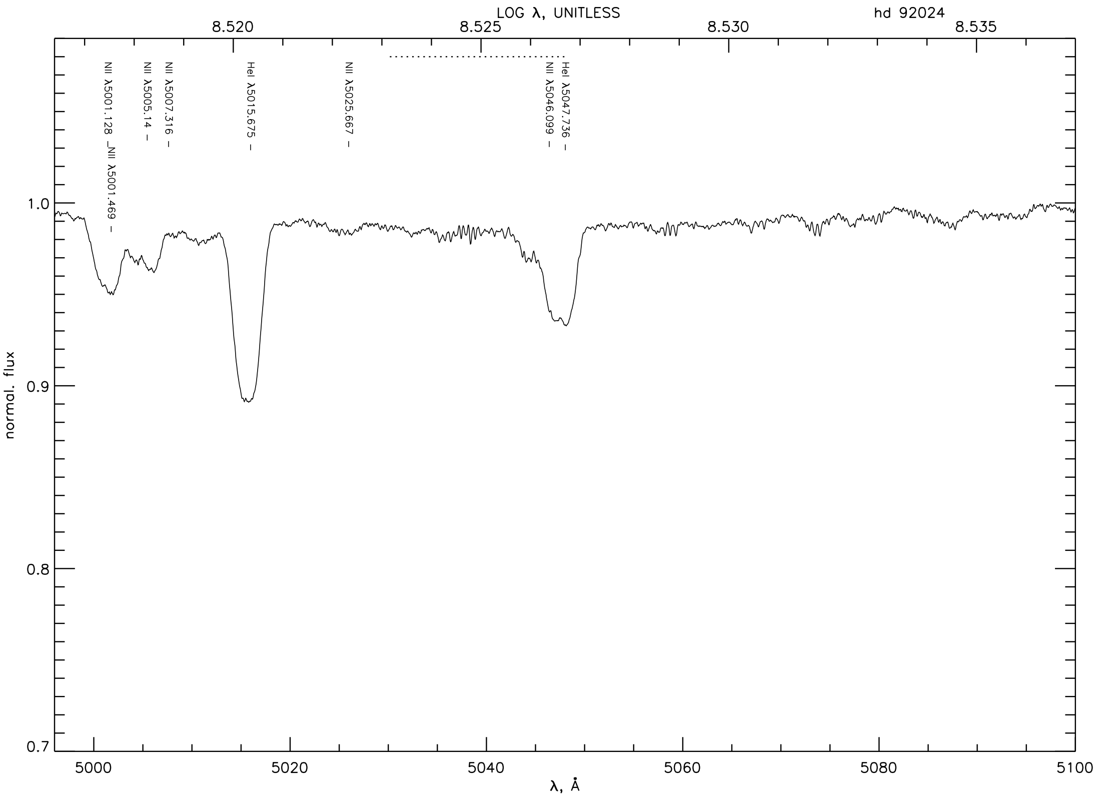
LOG λ, UNITLESS
hd 92024
8.520
8.525
8.530
8.535
NII λ5001.128
NII λ5001.469
NII λ5005.14
NII λ5007.316
HeI λ5015.675
NII λ5025.667
NII λ5046.099
HeI λ5047.736
normal. flux
1.0
0.9
0.8
0.7
5000
5020
5040
5060
5080
5100
λ, Å

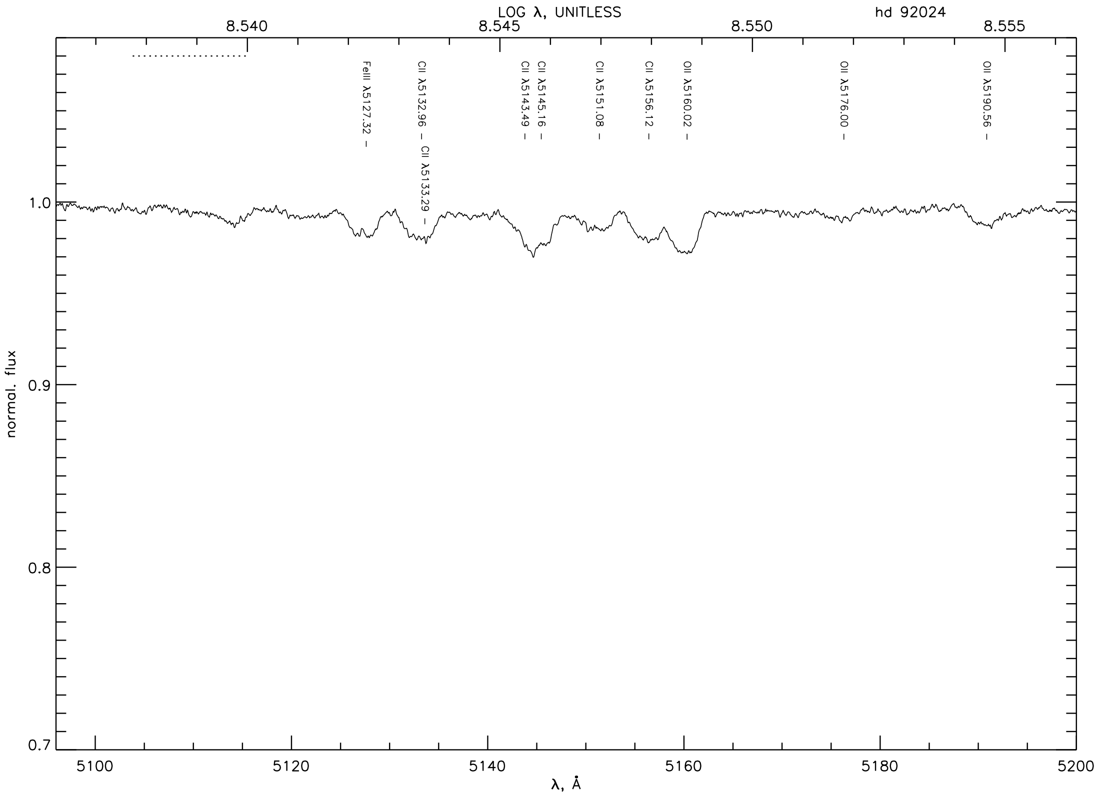
LOG λ, UNITLESS
hd 92024
8.540
8.545
8.550
8.555
FeIII λ5127.32
CII λ5132.96
CII λ5133.29
CII λ5143.49
CII λ5145.16
CII λ5151.08
CII λ5156.12
OII λ5160.02
OII λ5176.00
OII λ5190.56
normal. flux
1.0
0.9
0.8
0.7
5100
5120
5140
5160
5180
5200
λ, Å

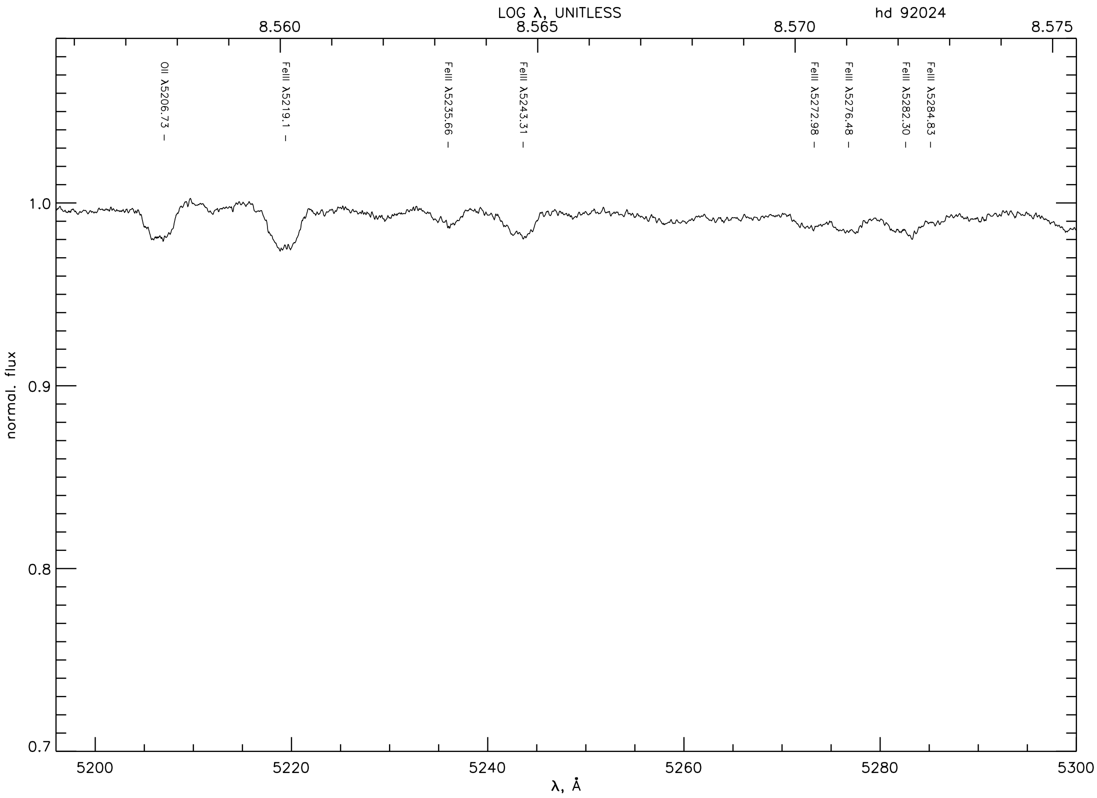
LOG λ, UNITLESS
hd 92024
8.560
8.565
8.570
8.575
OII λ5206.73
FeIII λ5219.1
FeIII λ5235.66
FeIII λ5243.31
FeIII λ5272.98
FeIII λ5276.48
FeIII λ5282.30
FeIII λ5284.83
normal. flux
1.0
0.9
0.8
0.7
5200
5220
5240
5260
5280
5300
λ, Å

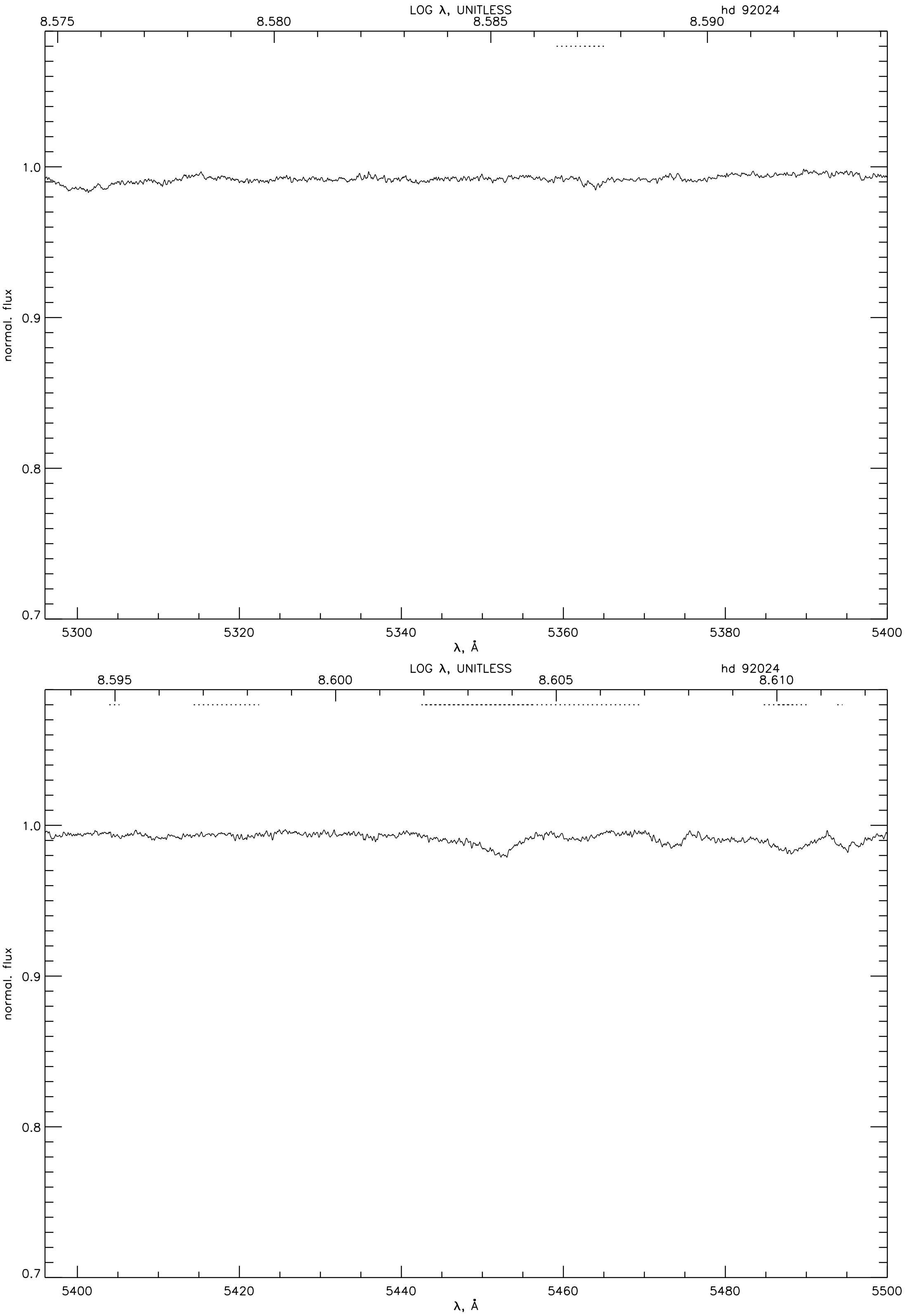

LOG λ, UNITLESS
hd 92024
8.575
8.580
8.585
8.590
normal. flux
1.0
0.9
0.8
0.7
5300
5320
5340
5360
5380
5400
λ, Å
LOG λ, UNITLESS
hd 92024
8.595
8.600
8.605
8.610
normal. flux
1.0
0.9
0.8
0.7
5400
5420
5440
5460
5480
5500
λ, Å

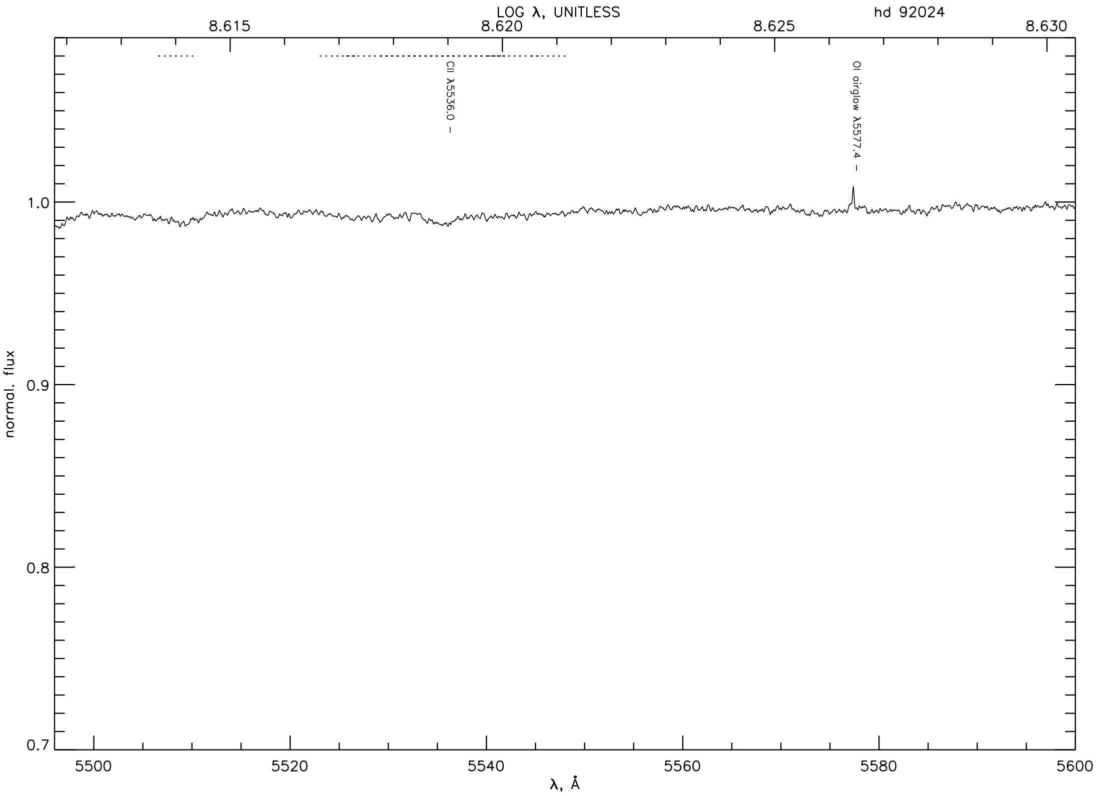
LOG λ, UNITLESS
hd 92024
8.615
8.620
8.625
8.630
CII λ5536.0
OI airglow λ5577.4
normal. flux
1.0
0.9
0.8
0.7
5500
5520
5540
5560
5580
5600
λ, Å

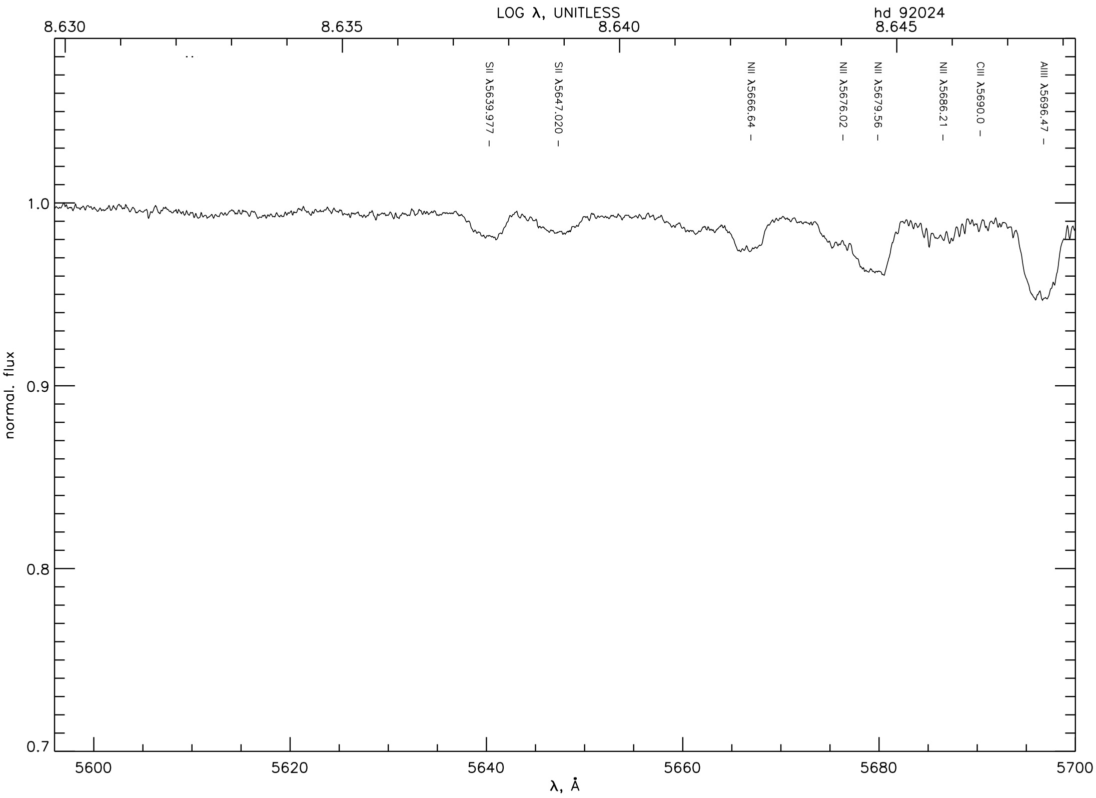
LOG λ, UNITLESS
hd 92024
8.630
8.635
8.640
8.645
SiII λ5639.977
SiII λ5647.020
NII λ5666.64
NII λ5676.02
NII λ5679.56
NII λ5686.21
CIII λ5690.0
AlIII λ5696.47
normal. flux
1.0
0.9
0.8
0.7
5600
5620
5640
5660
5680
5700
λ, Å

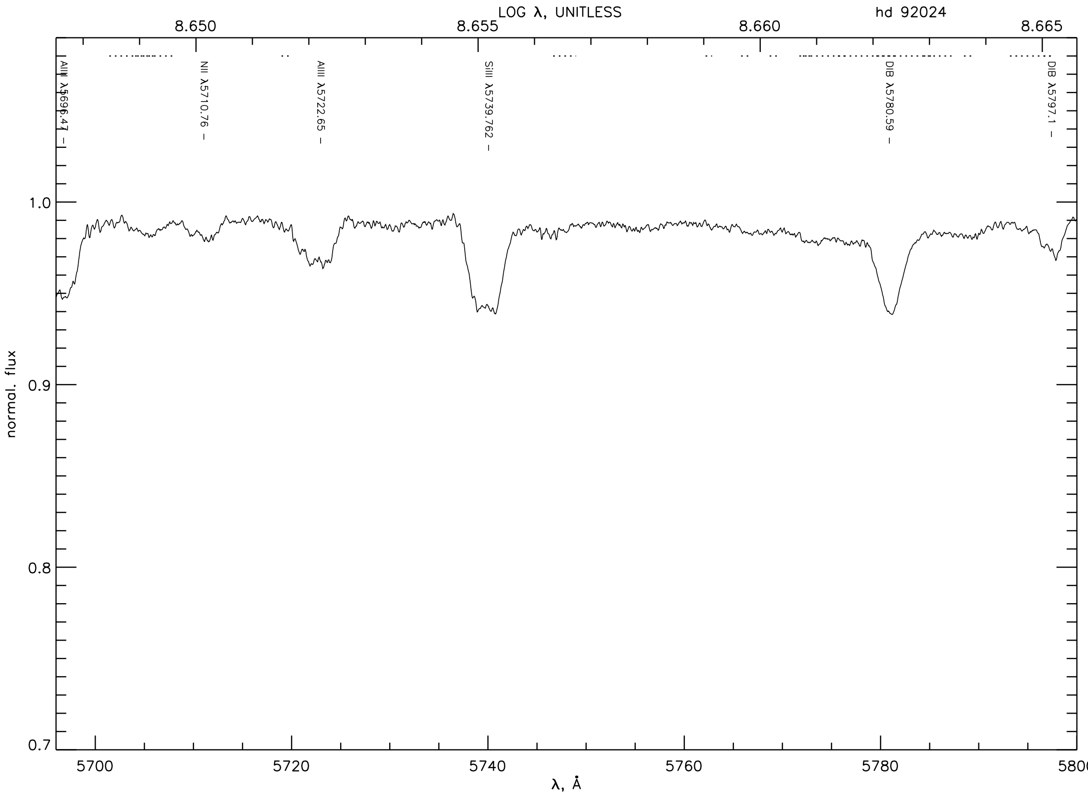
LOG λ, UNITLESS
hd 92024
8.650
8.655
8.660
8.665
AlIII λ5696.47
NII λ5710.76
AlIII λ5722.65
SiIII λ5739.762
DIB λ5780.59
DIB λ5797.1
normal. flux
1.0
0.9
0.8
0.7
5700
5720
5740
5760
5780
5800
λ, Å

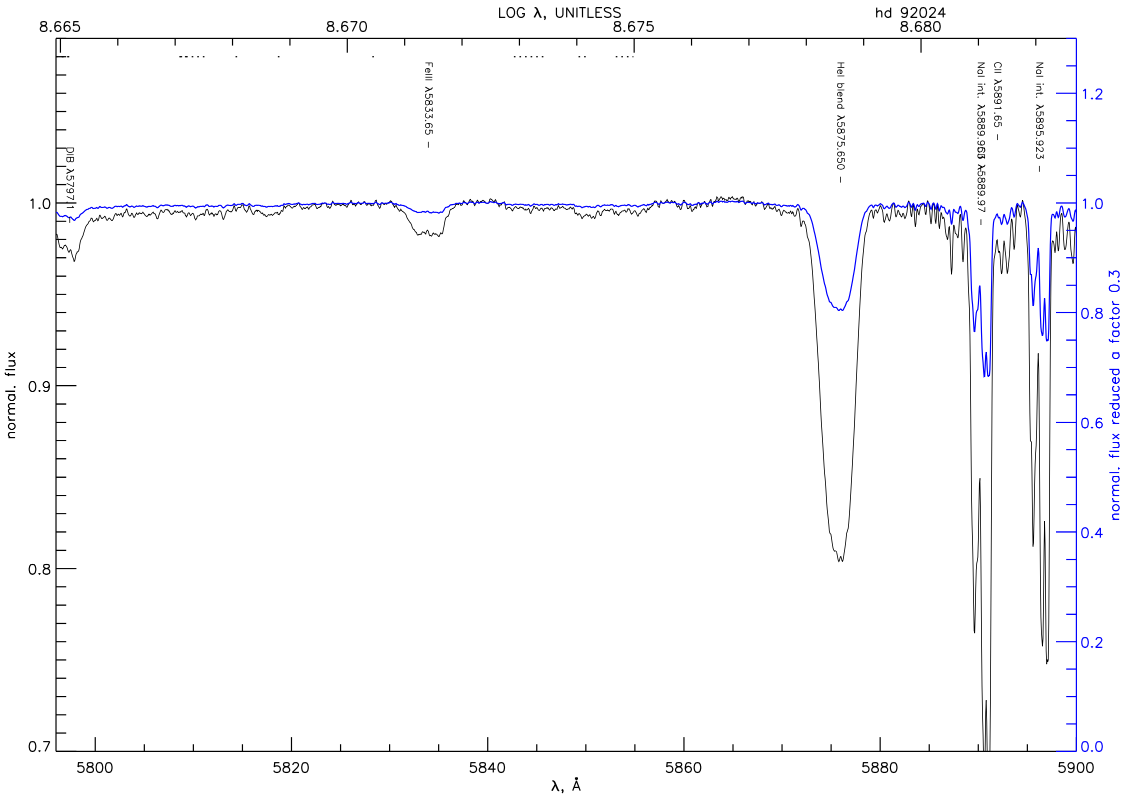
LOG λ, UNITLESS
hd 92024
8.665
8.670
8.675
8.680
DIB λ5797.1
FeIII λ5833.65
HeI blend λ5875.650
NaI int. λ5889.963 λ5889.97
CII λ5891.65
NaI int. λ5895.923
normal. flux
1.0
0.9
0.8
0.7
normal. flux reduced a factor 0.3
1.2
1.0
0.8
0.6
0.4
0.2
0.0
5800
5820
5840
5860
5880
5900
λ, Å

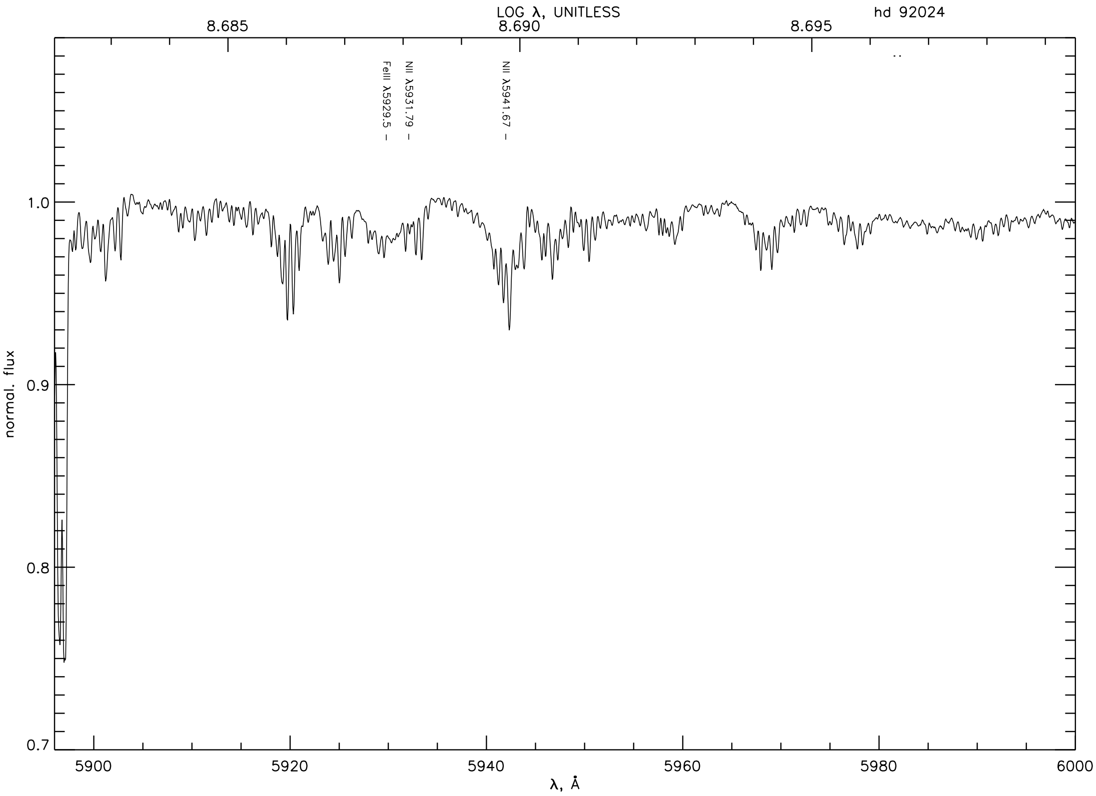
LOG λ, UNITLESS
hd 92024
8.685
8.690
8.695
FeIII λ5929.5
NII λ5931.79
NII λ5941.67
normal. flux
1.0
0.9
0.8
0.7
5900
5920
5940
5960
5980
6000
λ, Å

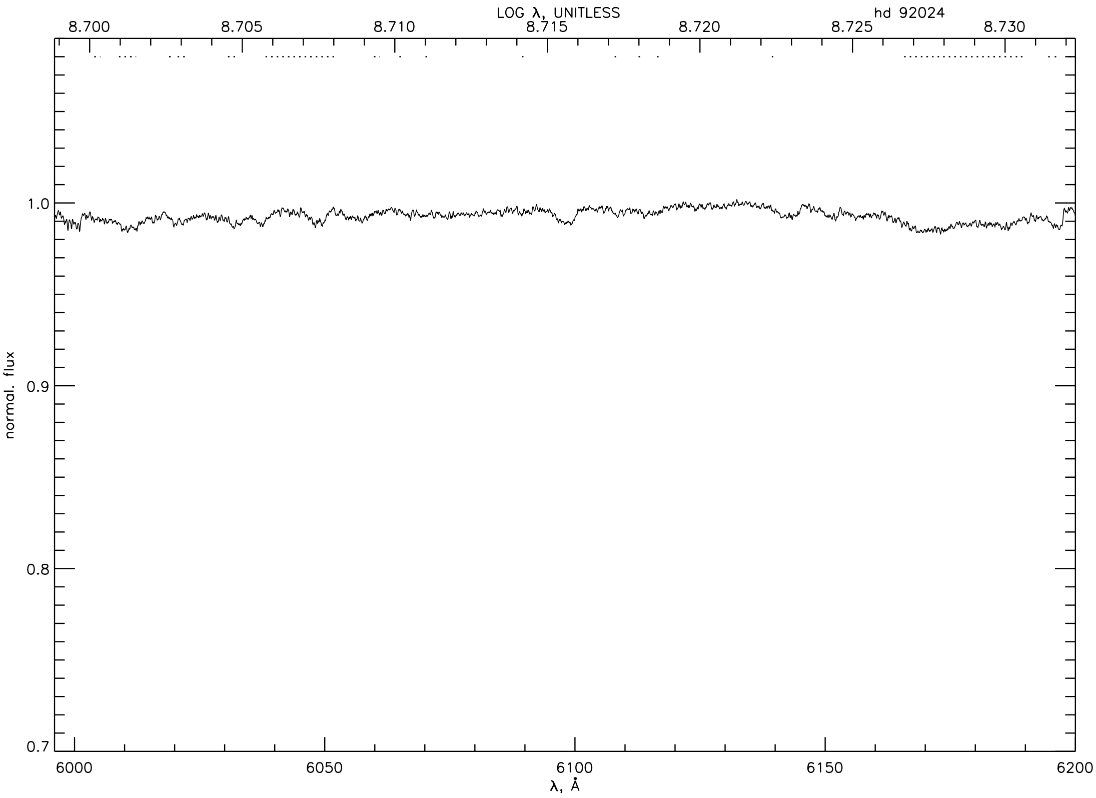
LOG λ, UNITLESS
hd 92024
8.700
8.705
8.710
8.715
8.720
8.725
8.730
normal. flux
1.0
0.9
0.8
0.7
6000
6050
6100
6150
6200
λ, Å

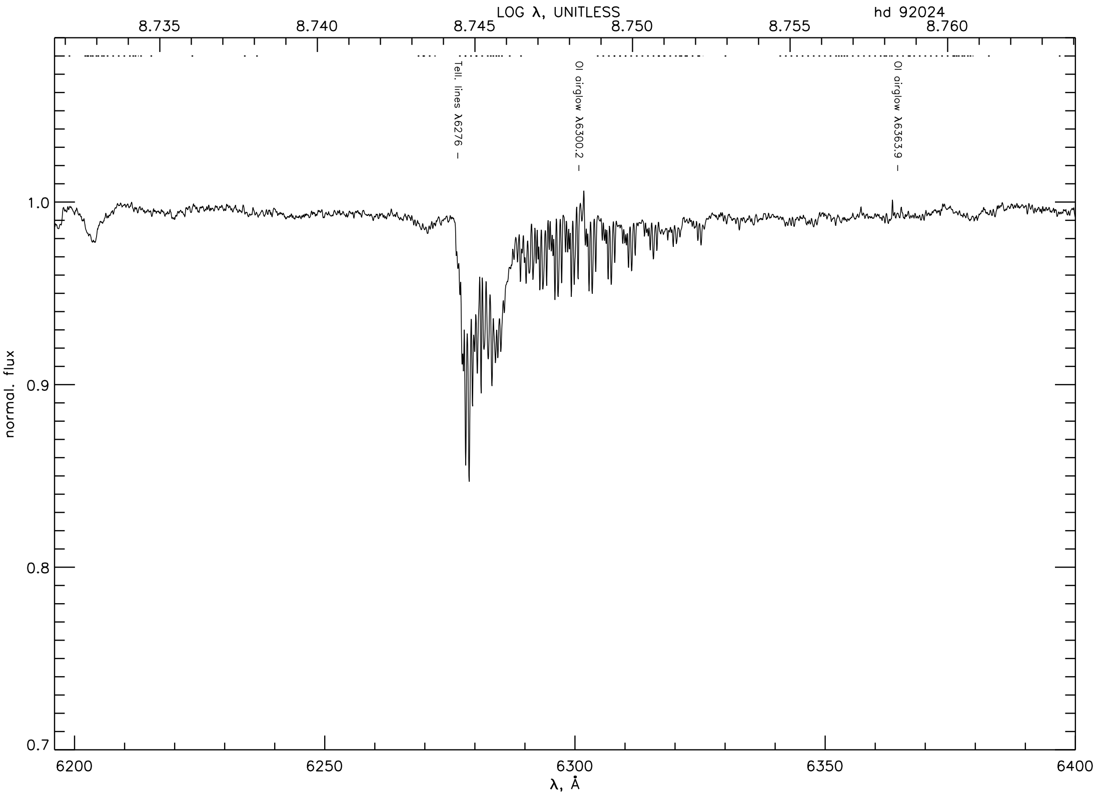
LOG λ, UNITLESS
hd 92024
8.735
8.740
8.745
8.750
8.755
8.760
Tell. lines λ6276 –
OI airglow λ6300.2 –
OI airglow λ6363.9 –
normal. flux
1.0
0.9
0.8
0.7
6200
6250
6300
6350
6400
λ, Å

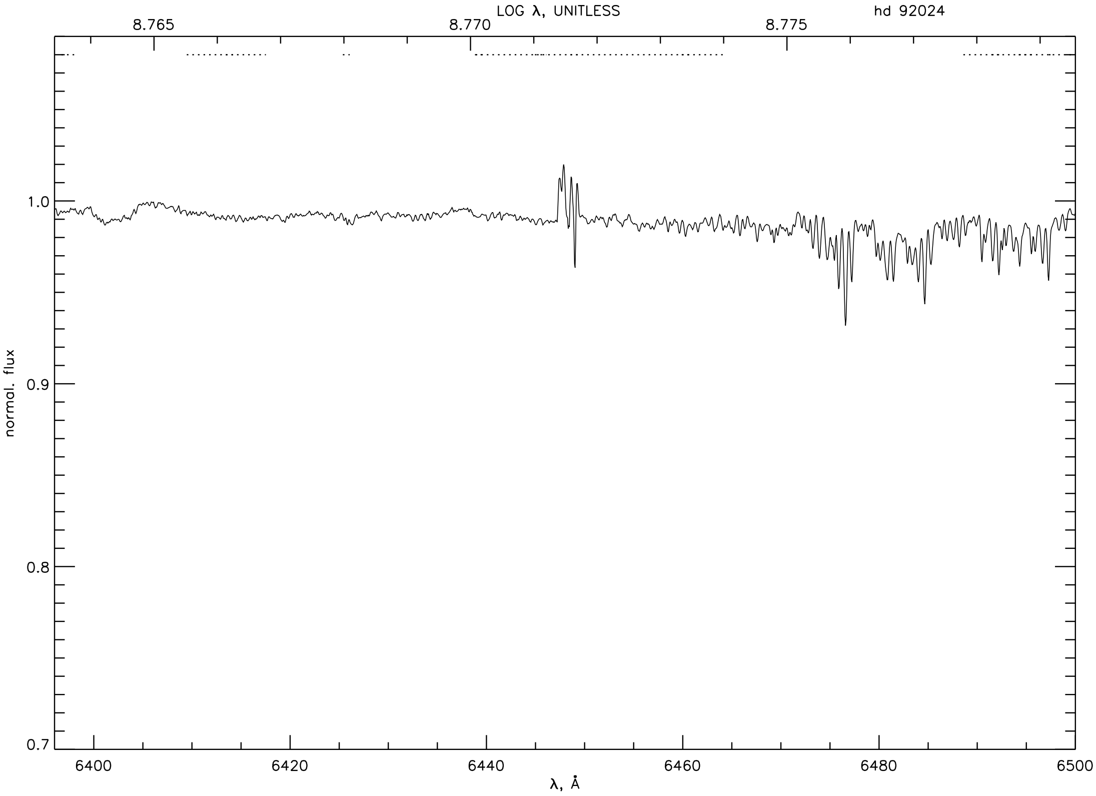
LOG λ, UNITLESS
hd 92024
8.765
8.770
8.775
normal. flux
1.0
0.9
0.8
0.7
6400
6420
6440
6460
6480
6500
λ, Å

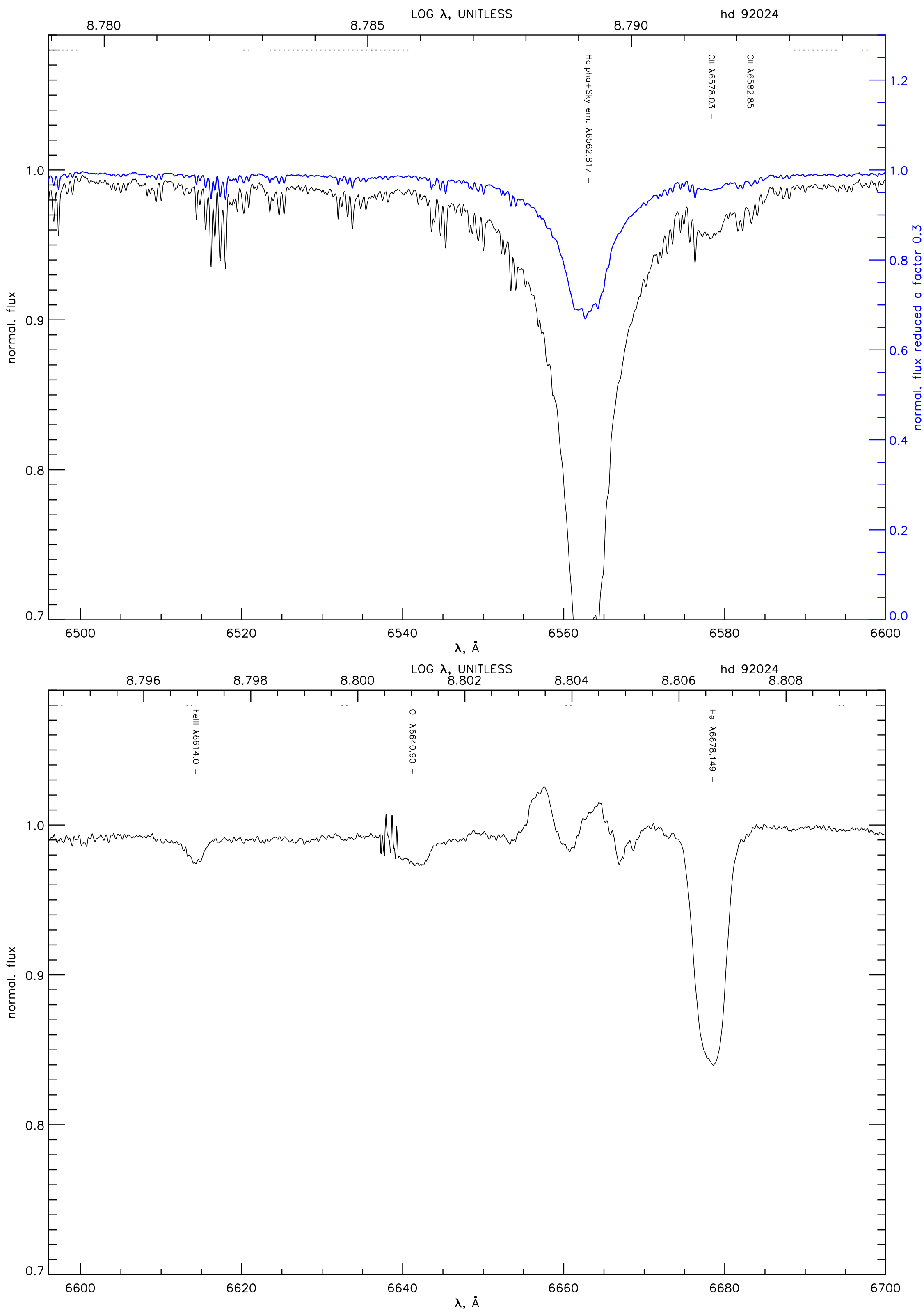
LOG λ, UNITLESS
hd 92024
Halpha+Sky em. λ6562.817
CII λ6578.03
CII λ6582.85
normal. flux
normal. flux reduced a factor 0.3
λ, Å
FeIII λ6614.0
OII λ6640.90
HeI λ6678.149

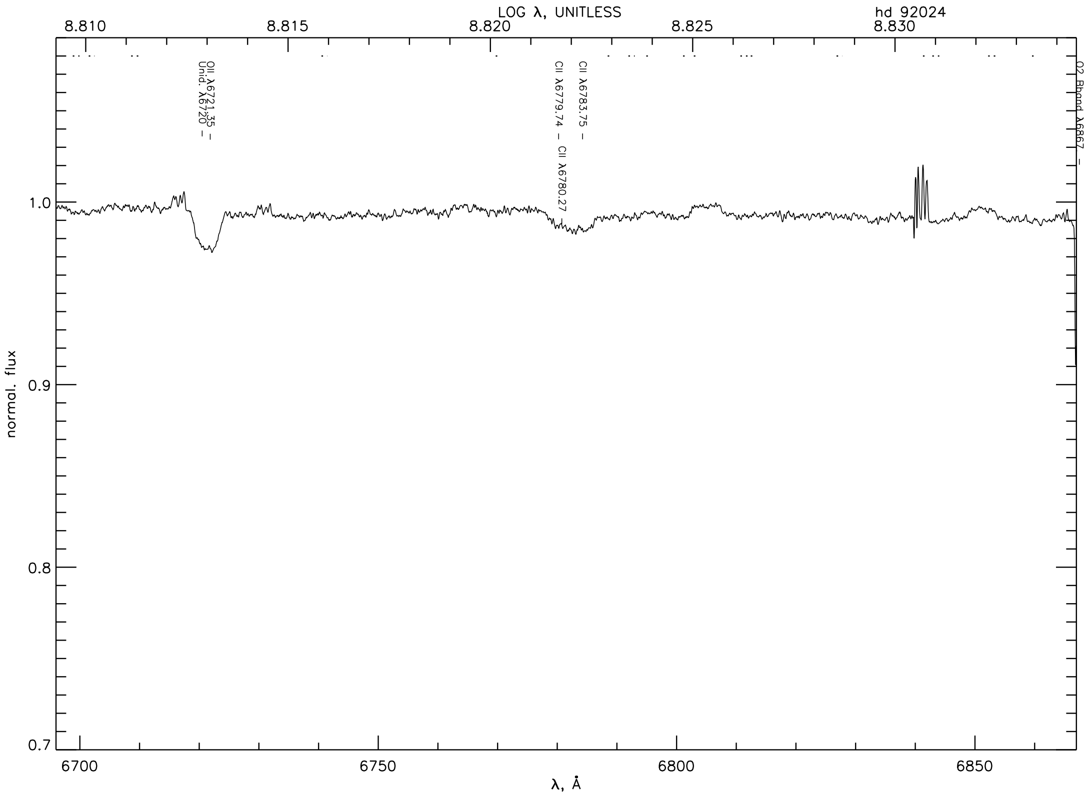
LOG λ, UNITLESS
hd 92024
8.810
8.815
8.820
8.825
8.830
OII λ6721.35
Unid. λ6720
CII λ6779.74
CII λ6780.27
CII λ6783.75
O2 Bband λ6867
normal. flux
1.0
0.9
0.8
0.7
6700
6750
6800
6850
λ, Å

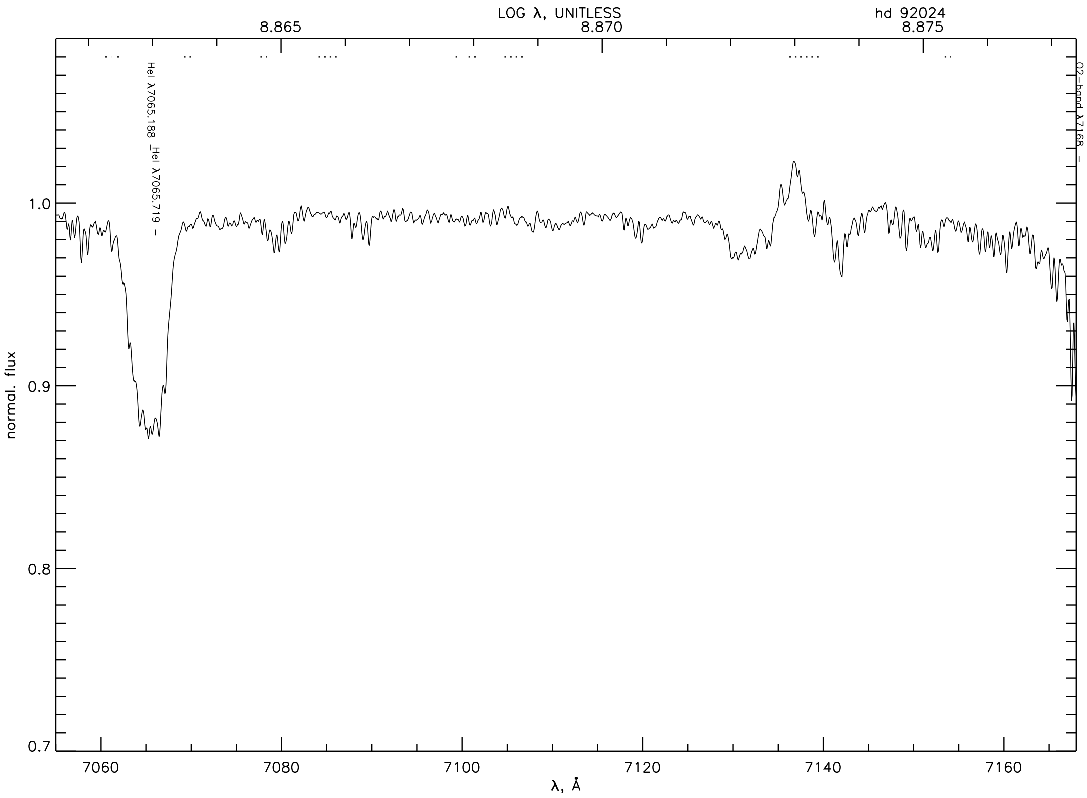
LOG λ, UNITLESS
hd 92024
8.865
8.870
8.875
HeI λ7065.188
HeI λ7065.719
O2-band λ7168
normal. flux
1.0
0.9
0.8
0.7
7060
7080
7100
7120
7140
7160
λ, Å

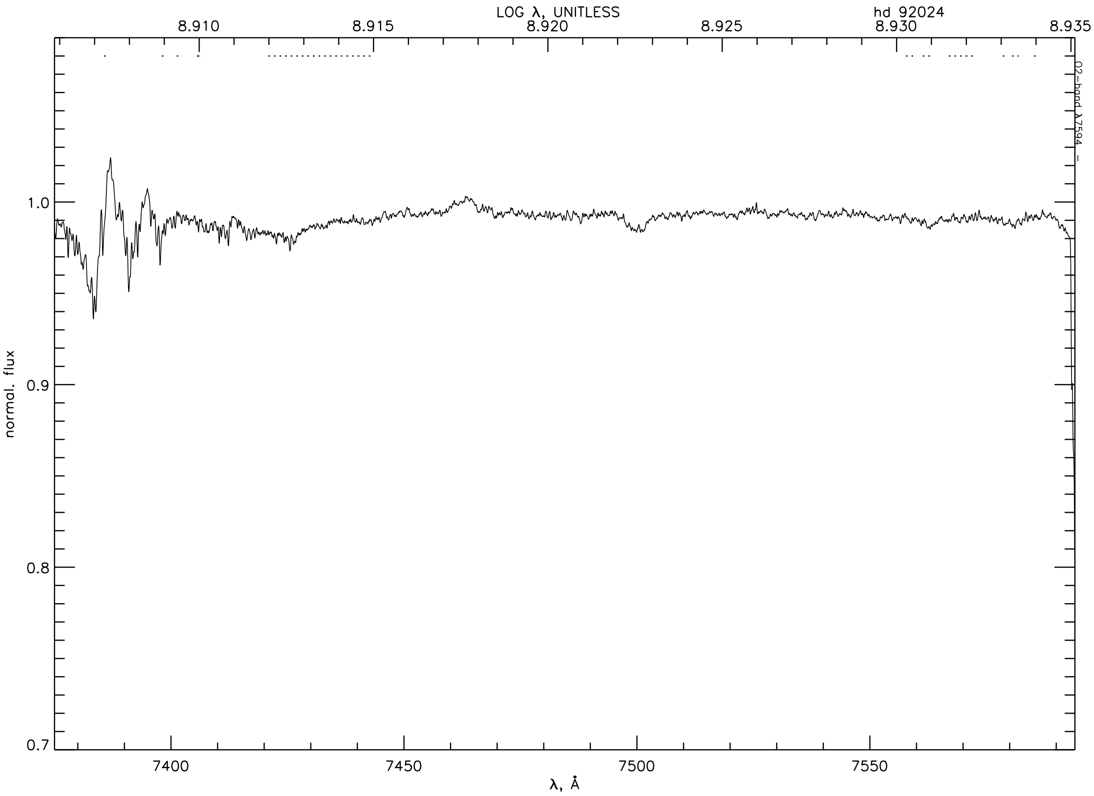
LOG λ, UNITLESS
hd 92024
8.910
8.915
8.920
8.925
8.930
8.935
O2-band λ7594 –
normal. flux
1.0
0.9
0.8
0.7
7400
7450
7500
7550
λ, Å

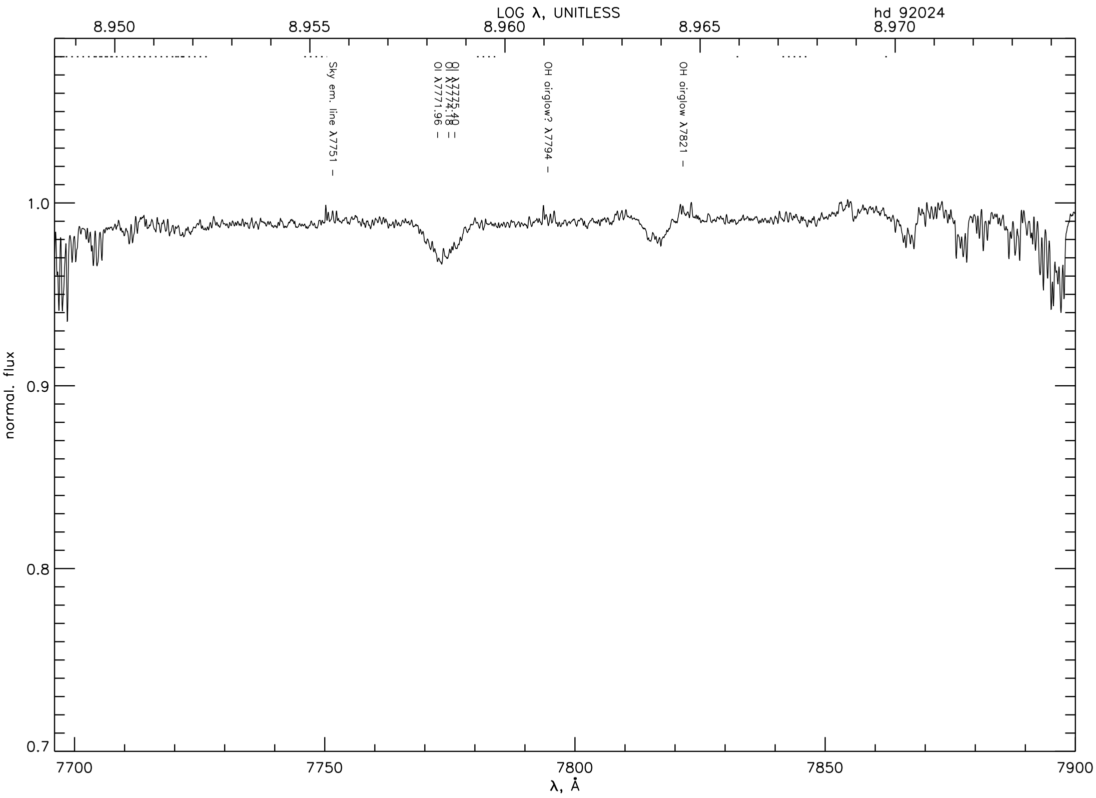
LOG λ, UNITLESS
hd 92024
8.950
8.955
8.960
8.965
8.970
Sky em. line λ7751 –
OI λ7775.40 –
OI λ7774.18 –
OI λ7771.96 –
OH airglow? λ7794 –
OH airglow λ7821 –
normal. flux
1.0
0.9
0.8
0.7
7700
7750
7800
7850
7900
λ, Å

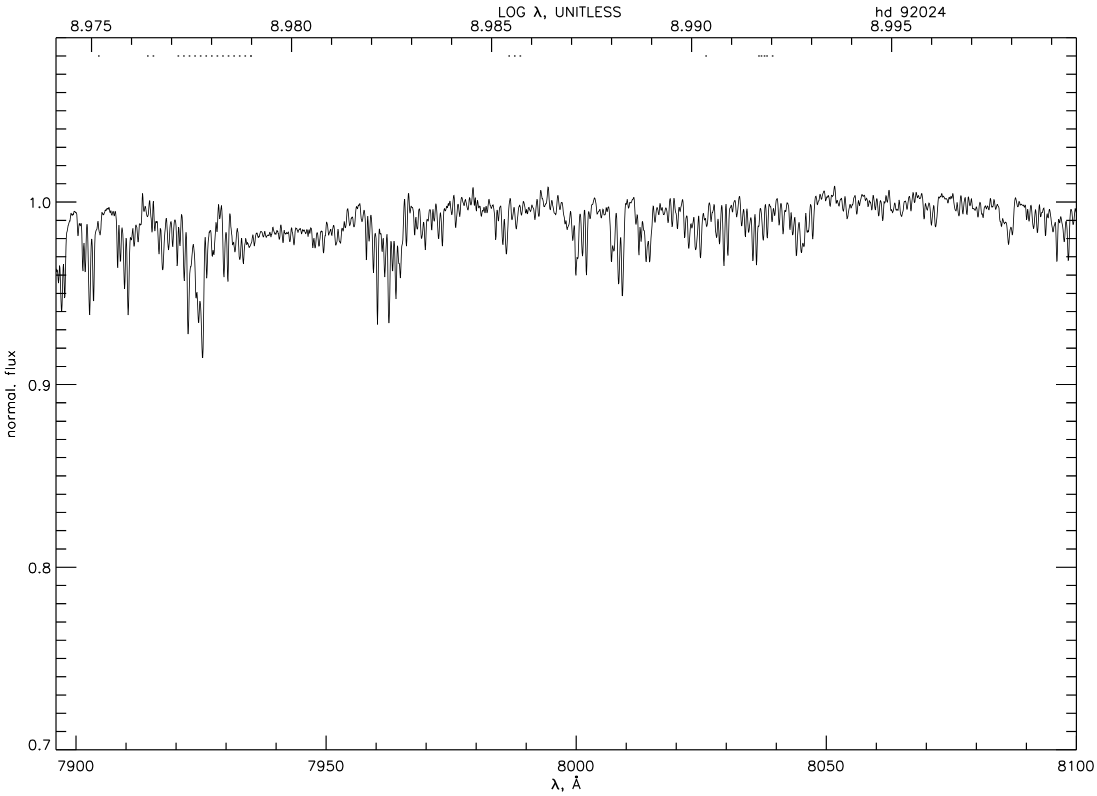
LOG λ, UNITLESS
hd 92024
normal. flux
λ, Å

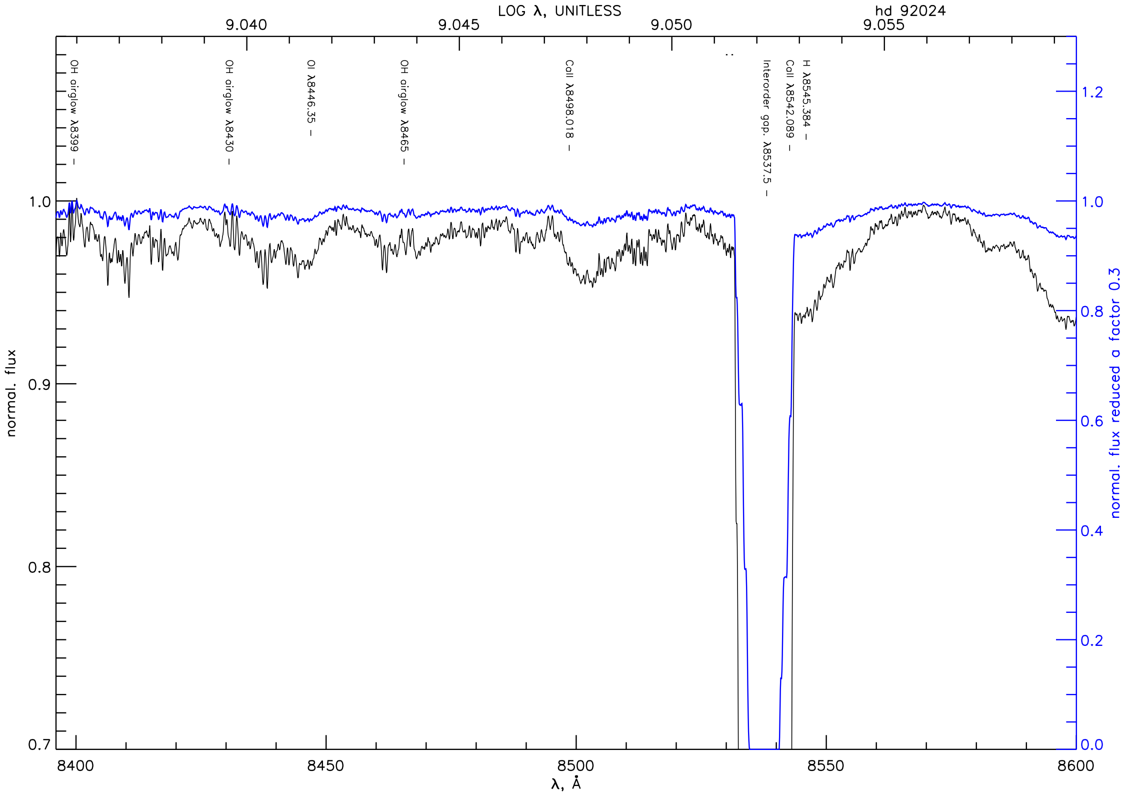
LOG λ, UNITLESS
hd 92024
OH airglow λ8399 –
OH airglow λ8430 –
OI λ8446.35 –
OH airglow λ8465 –
CaII λ8498.018 –
Interorder gap. λ8537.5 –
CaII λ8542.089 –
H λ8545.384 –
normal. flux
normal. flux reduced a factor 0.3
λ, Å

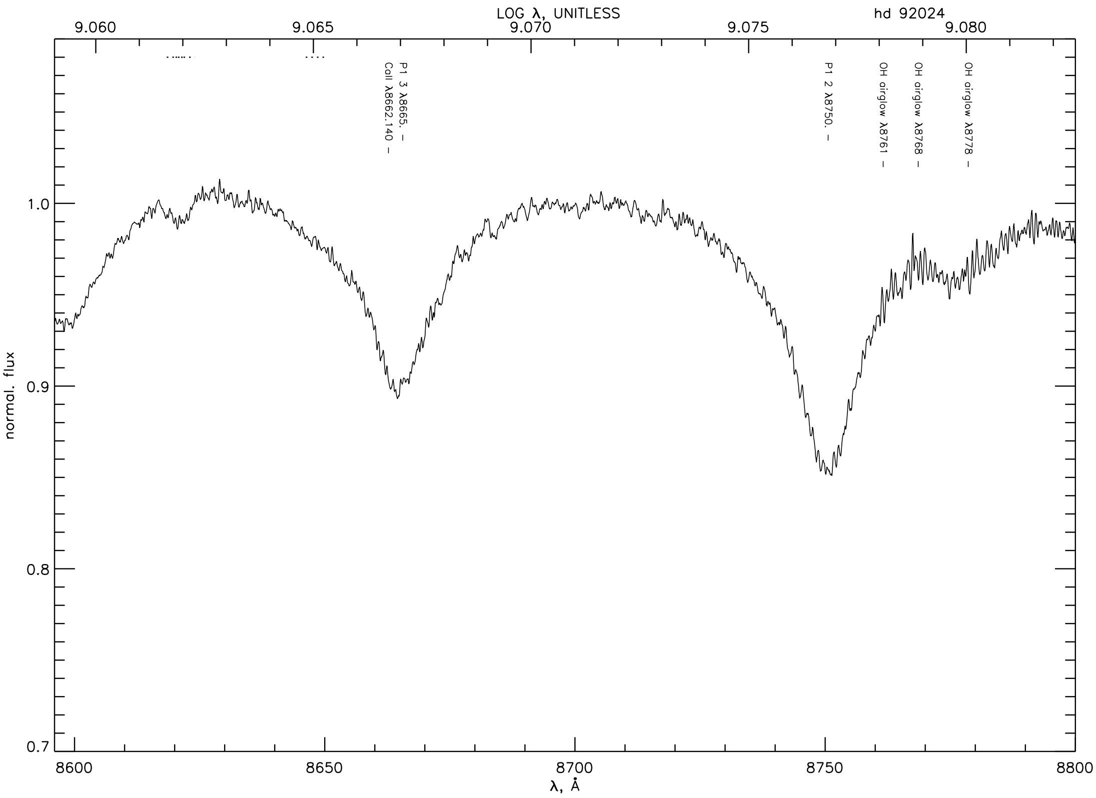
LOG λ, UNITLESS
hd 92024
9.060
9.065
9.070
9.075
9.080
P1 3 λ8665. –
CaII λ8662.140 –
P1 2 λ8750. –
OH airglow λ8761 –
OH airglow λ8768 –
OH airglow λ8778 –
normal. flux
1.0
0.9
0.8
0.7
8600
8650
8700
8750
8800
λ, Å